



NTNU – Trondheim
Norwegian University of
Science and Technology

Stability of the Graphite Electrode for Li-ion Batteries

Ingrid Roten Mattson

Chemical Engineering and Biotechnology

Submission date: July 2013

Supervisor: Ann Mari Svensson, IMTE

Co-supervisor: Carl Erik Lie Foss, IMT

Norwegian University of Science and Technology
Department of Materials Science and Engineering

Declaration

I hereby declare that this work has been performed independently and in accordance with the rules and regulations of the Norwegian University of Science and Technology (NTNU).

Ingrid Roten Mattson

Trondheim, July 1, 2013

Preface

This thesis was conducted at the Department of Materials Science and Engineering at the Norwegian University of Science and Technology (NTNU), during the spring semester 2013.

The experiments conducted as part of this thesis were carried out by the author with four exceptions: The nitrogen adsorption measurements, the electrolytes preparation and the casting of the Elkem graphite material were conducted by PhD candidate and co-supervisor Carl Erik Lie Foss, while the particle size distribution measurements were carried out by the staff at Elkem Carbon.

I would like to thank my main supervisor Professor Ann Mari Svensson at NTNU for guidance and support with the thesis work. Furthermore, I would like to thank PhD candidate and co-supervisor Carl Erik Lie Foss for conducting the nitrogen adsorption measurements, for preparing the electrolytes, for casting the Elkem graphite material, for assistance in the lab and for guidance and support with the thesis work. I would also thank Elkem Carbon for measuring the particle size distributions, PhD candidate Ahmet Oguz Tezel for lab advices, Senior Engineer Julian Tolchard for SEM training, PhD candidate Gerhard Olsen for help with Latex and the staff for always being very helpful.

Abstract

This thesis has focused on the characterization of two different graphite materials, in order to gain an improved understanding of how composition of the electrolyte and cycling of the battery influences the stability of the graphite electrode. The effect of the amount of the electrolyte solvent ethyl carbonate was emphasized. In addition, the thermal stability of the electrodes have been investigated by differential scanning calorimetry. Basic characterisations of the materials were conducted, among them scanning electron microscopy investigations, particle size distribution measurements and nitrogen adsorption measurements. Battery test cells was manufactured and cycled at different rates for 52 cycles to reveal the electrochemical performance of the materials and electrolytes. Electrochemical impedance spectroscopy was utilized to reveal possible degradation mechanisms causing capacity fade of the graphite electrodes.

It was found that the moderate cycled Elkem A2 (2650) graphite had the best retained capacity after 52 cycles. The electrolyte with the highest amount of ethyl carbonate (40 %) was found to create a stable SEI layer, as evidenced by electrochemical impedance spectroscopy. The capacity fade of the graphite electrodes was found to be due to increased electrolyte resistance and contact resistance and to an increased charge transfer resistance. The Elkem graphite showed the best thermal stability due to its higher amount of non basal plane to basal plane surface areas.

Sammendrag

Denne masteroppgaven har fokusert på karakterisering av to ulike grafittmaterialer, for å oppnå økt forståelse for hvordan sammensetningen til elektrolytten og syklingen av batteriet påvirker stabiliteten av grafittlektroden. Effekten av mengden av løsningsmiddelet etylkarbonat ble vektlagt. I tillegg ble den termiske stabiliteten til elektrodene undersøkt med såkalt differensiell skanning kalorimetri. Grunnleggende materialkarakterisering ble gjennomført, blant dem skanning elektron mikroskopi, partikkelstørrelsesmålinger og nitrogen adsorpsjonsmålinger. Batteritestceller ble satt sammen og syklet med ulike hastigheter opp til 52 sykler for å avdekke den elektrokjemiske ytelsen til materialene og elektrolyttene. Elektrokjemisk impedans spektroskopi ble brukt til å avsløre mulige degraderingsmekanismer som forårsaker kapasitetstap.

Det ble funnet at den moderat syklede grafitten Elkem A2 (2650) hadde den beste bevarte kapasiteten etter 52 sykler. Elektrolytten med høyest mengde etylkarbonat (40 %) dannet et stabilt SEI lag. Dette ble bevist ved hjelp av elektrokjemisk impedans spektroskopi. Kapasitetstapet til grafittlektroden ble funnet å være forårsaket av økt elektrolyttmotstand og kontaktmotstand, og en økt ladningsoverføringsmotstand. Grafitten fra Elkem hadde best termisk stabilitet på grunn av et høyere ikke basal til basal plan forhold.

List of abbreviations

BET	Brunauer-Emmett-Teller
CPE	Constant phase element
DEC	Diethylene carbonate
DFT	Density functional theory
DMC	Dimethyl carbonate
DSC	Differential scanning calorimetry
EC	Ethylene carbonate
EIS	Electrochemical impedance spectroscopy
EMC	Ethyl methyl carbonate
ICL	Irreversible capacity loss
NMP	N-Methyl-2-pyrrolidinone
PC	Propylene carbonate
PSD	Particle size distribution
PVDF	Polyvinylidene fluoride
SEI	Solid electrolyte interface
SEM	Scanning electron microscopy
SOC	State of charge

Contents

1	Introduction	1
1.1	Motivation	1
1.2	Aim of this work	2
2	Theory	3
2.1	Electrochemical principles of the lithium-ion cell	3
2.2	Graphite electrode	5
2.2.1	Lithium intercalation into graphite	7
2.2.2	Nitrogen adsorption measurements	7
2.3	Electrolyte	9
2.4	Electrochemical performance of the graphite electrode	11
2.4.1	Solid electrolyte interface	11
2.4.2	Cell impedances	14
2.5	Degradation	16
2.6	Electrochemical stability	18
2.7	Thermal stability	21

2.7.1	Differential scanning calorimetry	26
3	Experimental procedures	29
3.1	Materials	29
3.1.1	Particle size distribution measurements	29
3.1.2	Scanning electron microscopy (SEM)	29
3.1.3	Nitrogen adsorption measurements	30
3.2	Electrochemical characterization	30
3.2.1	Electrode preparation	30
3.2.2	Electrolyte preparation	31
3.2.3	Cell assembly	31
3.2.4	Electrochemical cycling	35
3.2.5	Scanning electron microscopy of electrodes	36
3.2.6	Electrochemical impedance spectroscopy	37
3.3	Thermal analysis	38
3.3.1	DSC sample preparation	38
3.3.2	DSC analysis	39
4	Results	41
4.1	Material characterization	41
4.1.1	SEM	41
4.1.2	Particle size distribution measurements	42
4.1.3	Nitrogen adsorption measurements	43
4.2	Electrochemical measurements	44

4.3	Electrochemical impedance spectroscopy	52
4.4	Thermal analysis	57
5	Discussion	62
5.1	Materials characterization	62
5.2	Electrochemical measurements	63
5.3	Electrochemical impedance spectroscopy	67
5.4	Thermal analysis	68
6	Conclusion	71
	Bibliography	72

Chapter 1

Introduction

1.1 Motivation

Li-ion batteries are the state-of-the-art rechargeable battery system. They have desirable characteristics, such as high gravimetric and volumetric energy densities, excellent cycleability and long cycling life, as compared to other energy storing systems [1].

Increasing energy consumption, global warming and concerns about the environment have led to a high demand for renewable and clean energy sources which can substitute the traditional fossil fuels. However, the time variations in power output from energy sources such as solar and wind power requires a system for storing energy during excess production, which can deliver energy in times of energy deficit. Rechargeable batteries are among the most successful technologies for storage of clean electricity from these energy sources [2]. Li-ion batteries are also promising candidates for use in electrical vehicles, hybrid electrical vehicles and plug-in electrical vehicles [3]. In addition, many other applications, such as cell phones and laptops rely on electrical energy storage systems and conversion devices.

To meet the energy storage and performance demands of new and existing applications, there is a need for batteries with even higher performance and longer cycle lives. For instance, Li-ion batteries for electrical vehicles should have a high power output to accelerate the car, show minimal capacity loss after long-time

cycling and have an excellent stability both at low and high temperatures.

The performance of Li-ion batteries are intimately related to the electrode materials used [4]. Even though a variety of new anode materials were intensely investigated in recent years, graphite is still the most important material for the negative electrode in Li-ion batteries [5, 6].

The major challenges related to graphite electrodes are their electrochemical and thermal stability. Several degradation mechanisms causes capacity fade during long-term cycling [7]. There is also a need for improved thermal stability. Thermal instabilities in Li-ion batteries have led to several cases in media reporting Li-ion batteries catching fire. The present year, media reported that Li-ion battery packs caught fire on board of the new 787 Dreamliner planes from Boeing. The reason for batteries catching fire is a phenomenon called 'thermal runaway'. It is known that the thermal stability of the graphite electrode is critical to this phenomenon, as thermal reactions in the graphite electrode arises at temperatures below 100 °C. These reactions might induce much higher heat evolution from reactions at the positive electrode, causing the battery to catch fire or even explode. This is an important safety issue which has become the subject of several studies [8].

1.2 Aim of this work

This work will focus on the characterization of two different graphite materials, in order to gain an improved understanding of how composition of the electrolyte and cycling of the battery influences the stability of the graphite electrode. The materials have been characterized to determine the morphology, particle size distributions and specific surface areas. Long-term electrochemical cycling at various rates and electrochemical impedance spectroscopy have been conducted to find connections between the materials properties, electrolyte properties and electrochemical performance of the graphite electrode. Thermal stability was characterized by so-called 'differential scanning calorimetry'. Attempts will be made to explain any observed differences between the materials and electrolytes.

Chapter 2

Theory

2.1 Electrochemical principles of the lithium-ion cell

Lithium ion batteries belong to the classes of rechargeable batteries. A schematic illustration of the operation of a Li-ion battery cell is provided in Figure 2.1.

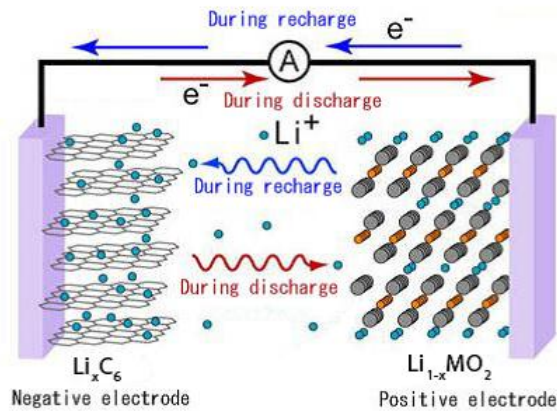


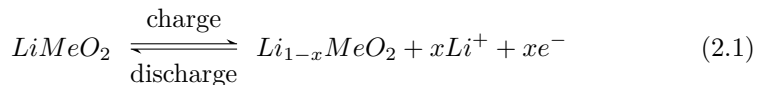
Figure 2.1: A schematic illustration of the Li-ion cell [9].

The battery cell consists of two electrodes separated by an electrolyte and a thin porous membrane. The electrodes contain the active material where the energy is stored. The state-of-the-art Li-ion battery is a so-called 'rocking-chair' battery, where Li-ions move back and forth between the negative and positive electrodes during cycling. The active materials of the electrodes are insertion materials, which act as host lattices for the Li-ions. The most common active material for the negative electrode is graphite, while transition metal oxides and phosphates have been mostly employed as active material for the positive electrode. Among the transition metal oxides and phosphates, LiCoO_2 , LiMn_2O_4 and LiFePO_4 are the most common ones [10].

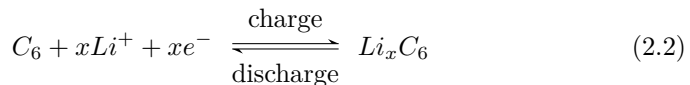
Upon discharge, the battery converts chemical energy into electrical energy. The energy is converted through chemical reduction-oxidation (redox) reactions at the electrodes. At the negative electrode electrons are liberated by the oxidation reaction. The electrons flow through an external circuit, where they can do useful work, before they enter the positive electrode and participate in a reduction reaction. The electrolyte is electronically insulating and prevents direct flow of electrons between the electrodes. Simultaneously, the electrolyte provides negative and positive ions (anions and cations) which migrate to the oppositely charged electrodes to maintain charge balance of the battery cell. A thin, porous separator (membrane) made of an electronically insulating material prevents the electrodes from physically touching each other, and hence prevents short-circuiting of the cell.

The electrochemical redox reactions can be described as follows [5], here with LiMO_2 (M = transition metal):

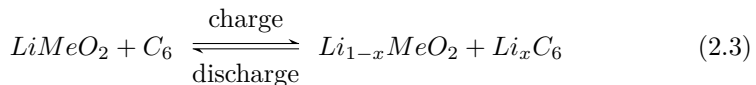
Positive electrode:



Negative electrode:



Total cell reaction:



The cell voltage is determined by the difference in the chemical potential of lithium in the two hosts [11]:

$$V = -\frac{\mu_{Li,cathode} - \mu_{Li,anode}}{e} \quad (2.4)$$

The average cell voltage is around 3.5 V [5]. To provide the desired voltage or capacity, the battery consists of one or several cells in series or parallel, respectively [1].

Upon recharging the redox reactions are forced in the reverse direction by an externally applied voltage which exceeds the internal electrochemical potential difference of the battery cell. Then, electrical energy is converted to chemical energy, which is stored in the active material of the electrodes.

2.2 Graphite electrode

The graphite electrode consists of micrometer sized graphite particles (active material) held together by a binder, creating a porous electrode. Carbon black is also mixed into the electrode to increase the electrical conductivity. The small sized particles and the porosity of the electrode is vital to achieve a large active surface area and short diffusion distances inside the particles, thus providing high kinetics and high rate capability [12].

Ideal graphite has a layered lattice structure with a perfect stacking order of graphene layers. A schematic illustration of graphite is provided in Figure 2.2. Each graphene layer consists of carbon atoms arranged in hexagonal rings. Only weak van der Waals forces exist between these layer planes. The usual stacking sequence of the graphene layers is ABABA... for hexagonal graphite, while for the less common rhombohedral graphite the stacking sequence is ABCABC.... Due to the small energy required for the transformation of hexagonal graphite into rhombohedral graphite (and vice versa), perfectly stacked graphite crystals are practically not available. Therefore, the term 'graphite' is commonly used regardless of the stacking order [13, 14].

Graphite has two distinct surfaces, the basal plane surface and the edge plane surface. The interlayer distance in graphite is 0.3354 nm in the *c*-axis direction (perpendicular to the layer planes), while the C-C bond distance in the *a*-axis direction (parallel to the layer planes) is 0.142 nm.

Most graphitic materials deviate more or less from the perfect graphite structure. A carbon particle is assumed to be a collection of crystallites, as illustrated

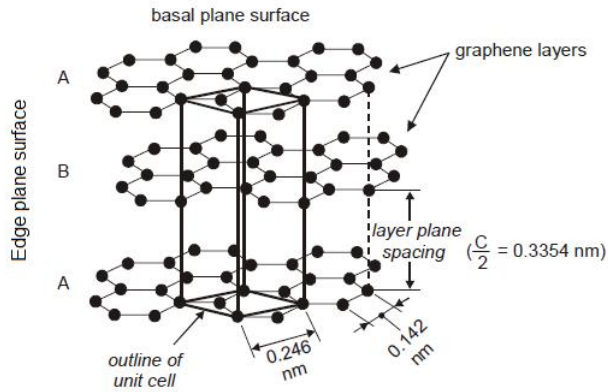


Figure 2.2: A schematic illustration of hexagonal graphite. Modified from [13].

in Figure 2.3. The crystallites are assumed to be stacked in some regular arrangement, but the individual crystallites may be tilted with respect to each other. This stacking arrangement allows for voids between the crystallites [15]. The crystallite sizes are defined by the structural parameters L_c (crystallite size in the direction perpendicular to the basal plane) and L_a (crystallite size in the direction parallel to the basal plane).

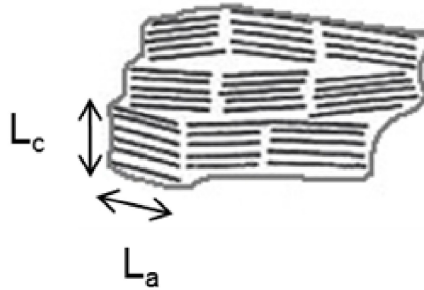


Figure 2.3: A schematic illustration of a graphite particle.

2.2.1 Lithium intercalation into graphite

Lithium intercalation proceeds via the edge plane surface of the graphite, intercalation through the basal plane surface can only occur at defect sites. The intercalation occurs in stages. The stage index n characterizes the number of graphene layers between two successive intercalated layers. Staging is a thermodynamic phenomenon caused by the considerable amount of energy which is required to 'open' the gap between two adjacent graphene layers. This staging phenomenon is thoroughly studied, and the following stages have been recognized: stage-4 (composition not well defined), stage-3 (LiC_{24}), a dilute lattice gas disordered stage-2 (LiC_{18}), stage-2 (LiC_{12}) and stage-1 (LiC_6) [12, 13].

The staging phenomenon can be seen in voltage-charge curves, like the one shown in Figure 2.4. The reversible Li-ion intercalation/de-intercalation occurs at potentials below ~ 0.2 V versus Li/Li^+ . The observed voltage plateaus in this potential region correspond to the phase transitions between successive stage- n phases during the Li-ion intercalation/de-intercalation. The transitions have been found to occur at 0.20, 0.14, 0.12 and 0.09 V versus Li/Li^+ , respectively, during intercalation [12]. During de-intercalation the transitions occur at slightly higher potentials.

During the intercalation reaction the stacking order of the graphene layers in graphite shifts to AAAA.... Due to intercalation of lithium the interlayer distance between the graphene layers is increased by about 10 % [13]. For graphite materials with high structural order, provided that the insertion current is low enough, the theoretical charge capacity of 372 mAh/g of graphite can be obtained [5]. This corresponds to $x=1$ in Li_xC_6 .

2.2.2 Nitrogen adsorption measurements

The surface characteristics of powders are usually obtained from nitrogen adsorption measurements at liquid nitrogen temperature (77 K).

The adsorptive potentials obtained from the nitrogen adsorption measurements can be interpreted with different theories. The theories provides different mathematical models for the process of gas sorption. The Brunauer, Emmett and Teller (BET) theory assumes that nitrogen adsorbs homogeneously on the surface of the sample, i.e. all surface sites are equal. Basic surface characterizations, such as the specific surface area and micropore area can be obtained by applying this theory.

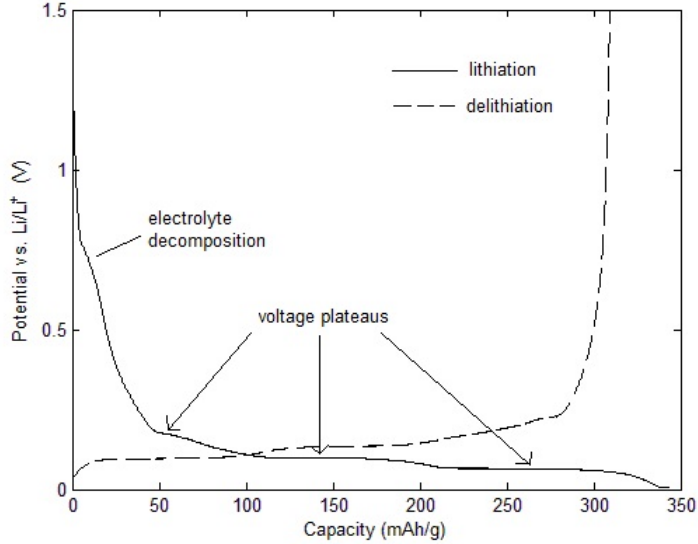


Figure 2.4: Typical voltage-charge curve of the first lithiation and delithiation of a Li/graphite half cell.

Density functional theory (DFT) assumes that basal, edge and defect sites have different adsorption energies, i.e. that the strength with which nitrogen adsorbs to a surface, varies for different surface types. One model was developed Ross and Olivier (Olivier2012), who ascribed the adsorptive potential distributions centred between 50 and 60 K to the basal plane surfaces. Generally, the magnitude of the adsorptive potential increases with the local density of adsorbent atoms. The edge plane has a lower areal density of carbon atoms and will adsorb nitrogen with a lower adsorptive potential than the basal planes (< 40 K). Defect surfaces, such as dislocations and surface steps result in an increased surface roughness and enhanced interactions between the surface atoms and the nitrogen atoms. Hence, the defect surfaces adsorb nitrogen with a higher adsorptive potential than the basal planes (> 62 K). By evaluating the contribution to the surface area at different adsorption energies/potentials, the relative ratio of the various surface types can be obtained.

2.3 Electrolyte

The electrolyte consists of two major components, namely solvents and salt, and many different combinations have been investigated for use in Li-ion batteries during the recent years. The fundamental requirements of the electrolyte is to have high ionic conductivity and good stability in the operating potential range of the battery.

The electrolyte should be electrochemically stable, i.e. remain inert during operation. This means it should be stable against both oxidative decompositions at the positive electrode surface and reductive decompositions at the negative electrode surface. This is achieved either by thermodynamic stability of all the components under the operating conditions, or by effective passivation of the electrode surfaces, preventing sustaining decomposition of the electrolyte components (the electrolyte components decompose into protective products). Because the voltage range of the Li-ion battery normally extends beyond the stability range of the electrolyte, stability is required by passivation for most Li-ion batteries. The passivating layer on the negative electrode surface is called the solid electrolyte interface (SEI) layer and will be further explained in the next chapter. The wide voltage window of the Li-ion battery (~ 3.5 V) demands the use of non-aqueous solvents. Today esters are almost exclusively used, due to their stability against oxidations and their ability to form a stable passivating interface upon reduction [16].

If the passivation is not efficient enough, co-intercalation of solvent molecules might take place, leading to exfoliation of the graphite particles. The solvent molecules co-intercalate along with the lithium ions between the graphene sheets of the graphite. This process breaks up the graphite structure, exposing fresh graphite to the electrolyte. The graphite exfoliation results in a drastic enlargement of the surface area in contact with the electrolyte. This leads to an ongoing electrolyte decomposition on this newly formed surface [10, 17].

The ionic conductivity of the electrolyte is related to the number of moles of the ions in the solution, and their mobilities and valence numbers. To ensure a high number of ions in the solution, the solvent should have a good ability to dissolve and coordinate the salt ions. This implies that the solvent should have a high dielectric constant (usually associated with high viscosity), while the salt should have a low dissociation energy (associated with a large size, which favours charge distribution and hence lower dissociation energy). On the contrary, high mobility of the ions in the solution requires a solvent with low viscosity and solvated ions with a small volume (small sized). These contradicting requirements can be

met by mixing one co-solvent of high dielectric constant with a co-solvent with low viscosity. The former solvent will be responsible for dissolving the salt and coordinating Li^+ , while the latter provides a conducting medium of low resistance for the solvated Li^+ ions [16].

Among the esters, the diesters of carbonic acid have been found especially suitable. Cyclic and linear carbonates possess high dielectric constant and low viscosity, respectively. Hence, the electrolytes used for commercial Li-ion batteries are based on a mixture of a cyclic carbonate (ethylene carbonate (EC) or propylene carbonate (PC)) with one or more linear carbonates (dimethyl carbonate (DMC), ethylmethyl carbonate (EMC) or diethyl carbonate (DEC)) [16]. Exfoliation of the graphite is common in PC based electrolytes [12, 18], while EC have been found to prevent exfoliation by forming a stable passivating film on the graphite surface [19].

The structural formulas of the above mentioned solvents are shown in Figure 2.5.

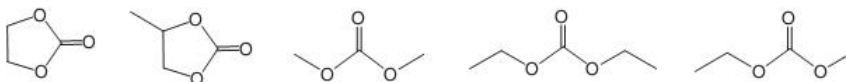


Figure 2.5: Structural formulas of important solvents. From left to right: EC, PC (cyclic carbonates), DMC, DEC, EMC (linear carbonates). Modified from [16].

Among the the salts, LiPF_6 is the industry standard in state-of-the-art lithium-ion batteries. The fluorinated inorganic anion is favored due to its superior dissolution and dissociation properties in non-aqueous solvents and its excellent ability to form a passivating interface on the positive electrode surface. Although widely used, the search for alternatives continues, because LiPF_6 is moisture sensitive and tend to be increasingly reactive at elevated temperatures [16].

Other important requirements is a wide liquid range (low melting points, high boiling points), ability to wet the separator, inertness towards other cell parts (binders, current collectors etc.), high safety and low toxicity [16].

2.4 Electrochemical performance of the graphite electrode

2.4.1 Solid electrolyte interface

As this work has focused on graphite materials, only the reduction of electrolyte components on the graphite electrode surface will be discussed. Due to the high potential window (3.5V and above) of Li-ion batteries, normal aqueous electrolytes cannot be used. To achieve stability in these systems one must use non-aqueous electrolytes, and even they are not completely stable in the high potential window. This is the reason why the electrolyte components are irreversibly reduced on the electrode surface during first cycle of operation. The electrolyte decomposition products form a passive layer on the electrode surface, named the solid electrolyte interface (SEI) layer. In an ideal case the SEI layer prevents further decomposition of the electrolyte by blocking the electron transport through it while simultaneously allowing Li-ions to pass through during cycling. This way the SEI layer provides kinetic stability to the electrolyte in the successive cycles and thereby ensures good cyclability to the electrode [10,20]. As the properties of this layer are fundamental for the functioning and the performance of the negative electrode, it has been the subject of extensive work [12].

The onset potential of SEI formation is not a fixed value, but 0.8 V versus Li/Li⁺ is the most widely adopted practical value. The SEI formation process is clearly visible on the galvanostatic curves as an irreversible plateau at a potential close to this value [10,12], as can be seen in Figure 2.4.

The picture of a real SEI inside the battery has always been blur. The general structural and morphological picture of the SEI that has emerged in recent years is one of a dense inorganic matrix close to the carbon and a porous organic or polymeric layer close to the electrolyte phase. The inorganic components are normally salt degradation products (ex. LiF, Li₂CO₃, Li₂O), while the organic components are partial or complete reduction products of the solvents of the electrolyte (ex. (CH₂OCO₂Li)₂, ROCO₂Li, ROLi) [10]. A schematic picture of a proposed structure of the SEI layer is shown in Figure 2.6.

Since Li⁺ is a limited resource in a Li-ion battery, the lithium trapped in the SEI layer are quantified as an 'irreversible capacity' [16]. This means that SEI formation must be as effective as possible to keep the charge losses as small as possible [22].

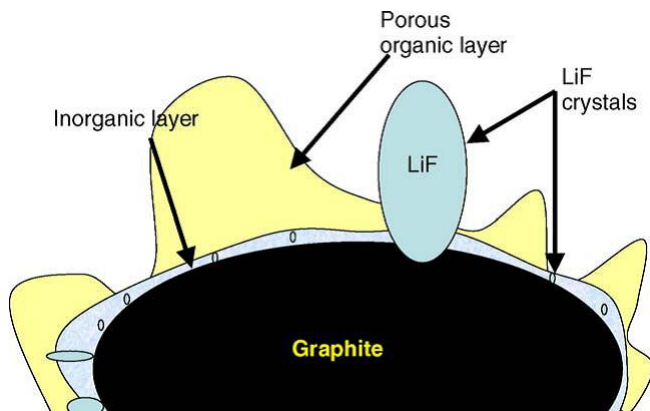


Figure 2.6: A schematic picture of the SEI on a graphite particle [21].

The largest irreversible growth of the SEI layer occurs during the first cycle, but at least five cycles are needed for a complete growth of the layer [23]. However, the composition and thickness of the SEI does not stay constant throughout cycling or storage. There are many different ways in which it can transform. It may partially dissolve in a solvent of the electrolyte, e.g., DMC [10]. Its thickness may also vary during cycling. Bryngelsson et al. [23] (2007) suggested that the SEI is dynamic, as they observed a thickening of the SEI layer at lower potentials (lithiated state) and a thinning-out of the layer at higher potentials (delithiated state). Typical SEI thicknesses ranges from a few Å to tens or hundreds of Å [10].

Since SEI is an interphase between the active material and the electrolyte, it is obvious that properties of both these phases dictates the composition, properties, efficiency and stability the SEI.

2.4.1.1 Effect of graphite on the SEI

SEI is essentially formed on the graphite surface, thus the type of graphite and its properties significantly affects the SEI. It is almost universally accepted in the literature that the irreversible charge loss occurring during the first cycle depends on the BET specific surface area of the graphite, because the SEI covers all the surface area exposed to the electrolyte solution. The specific surface area of the graphite increases by decreasing particle size, as the relative amount of surface atoms to bulk atoms increases. Joho et al. [22] showed that the irreversible

capacity loss caused by SEI formation during the first lithium intercalation in graphite negative electrodes was approximately linearly proportional to the BET specific surface area of the graphites.

Even though the surface is very important for SEI formation the importance of the crystallographic structure of the graphite should not be underestimated. Zheng et al. [24] (1999) found that the crystallographic structure and particle morphology are as influential as BET specific surface area. They showed that coke and graphite powders having same BET specific surface area exhibit different irreversible capacity losses. Edges and surface imperfections like defects, crevices, and active sites act as catalytic sites for solvent reduction. Dangling bonds and high current density on these sites favour electrolyte reduction. Thus concentration and nature of defects, and edge to basal plane ratio are also critical factors affecting SEI properties.

Placke et al. [25] (2012) investigated the importance of the ratio of basal planes to non-basal planes (edge planes and defects) on the irreversible capacity loss. They found that the irreversible capacity loss increases nearly linearly with an increasing ratio of non-basal plane surface area respective decreases with an increasing ratio of basal plane surface area. At the same time, they did not find a consistent linear relationship between the irreversible capacity loss and the specific surface area as measured by nitrogen adsorption and evaluated by the DFT method. In conclusion, the basal plane to non-basal plane ratio might have just as much significance on the irreversible capacity loss as the specific surface area.

Peled et al. (2004) studied SEI composition and morphology on a highly oriented graphite. They found that the solvents are preferentially reduced on the basal planes, while the salt anion is preferentially reduced on the edge planes. In addition, they observed that the SEI was thinner on the basal plane than on the edge plane.

2.4.1.2 Influence of the electrolyte composition on the SEI

As explained in chapter 2.3, the reduction compound of EC is believed to be responsible for a stable SEI which prevents exfoliation, making EC an essential cosolvent in Li-ion batteries. However, in recent years there have been some studies on the Li^+ solvation sheet and how the ratio of EC/linear carbonates could have an impact on which species are preferentially reduced to form the SEI, and hence the stability of the SEI layer [26, 27].

Xu et al. [26, 27] (2007) studied the impact of Li^+ solvation sheet structure

on the SEI chemistry. After cycling cells with graphite and electrolytes with different EC/DMC and EC/EMC ratios they studied the decomposition products in the SEI layer by means of NMR analysis. They found that linear carbonate originating species were hardly detectable in electrolytes with more than 30 % EC. In electrolytes with only 10 % EC the linear carbonate originating species were abundant. The authors suggested that the high dielectric constant of cyclic carbonates (like EC) results in a stronger interaction with Li^+ as compared to the linear carbonates. The stronger interaction between Li^+ and cyclic carbonate predicts a selective recruiting process of the inner solvation sheet. In most nonaqueous solvents, Li^+ possesses an average solvation number of 4. They authors suggested that the Li^+ should predominantly consist of EC in solutions where the bulk EC content is higher than 30 %, which ensures sufficient EC molecules for Li^+ to conscript. However, when the EC content is below 30 %, fewer than three EC molecules are averagely available for each Li^+ , and the linear carbonates would appear in the solvation sheet. The solvents bound in the inner solvation sheet will migrate with the Li^+ to the edge sites of the graphite, while the solvents which are not part of the solvation sheet are electro-neutral and can only get in contact with the graphite surface by diffusion. Hence, the solvents that are preferentially recruited into the solvation sheet of Li^+ are also preferentially reduced during the formation of the SEI. Based on the knowledge that EC is essential for a stable SEI, the authors suggest that an EC content below 40 % will result in a less stable SEI.

It should be mentioned that the proposed composition of the SEI might vary from one research group to another, due to different operating conditions in the laboratories. [10].

2.4.2 Cell impedances

Low cell impedances will yield a battery with high performance and rate capability. The available capacity might be reduced by an increased voltage drop due to a rise in cell impedance that prevents the battery from being fully discharged or charged at a specific current [28].

Several processes contribute to the total cell impedance; Li^+ conduction in the bulk electrolyte, stripping of the Li^+ solvation sheet, Li^+ diffusion/migration through the SEI layer, the expansion-contraction of lattice structure within the electrodes, Li^+ diffusion within the electrodes and the electron transfer from the external source to the host lattice of the electrodes [16]. The first three mentioned processes and Li^+ diffusion within the electrode are schematically

illustrated in Figure 2.7. Impedance analysis have discovered that the stripping of the Li^+ solvation sheet and Li^+ diffusion/migration within the SEI layer are main contributors to the impedance on the anode side [16, 29].

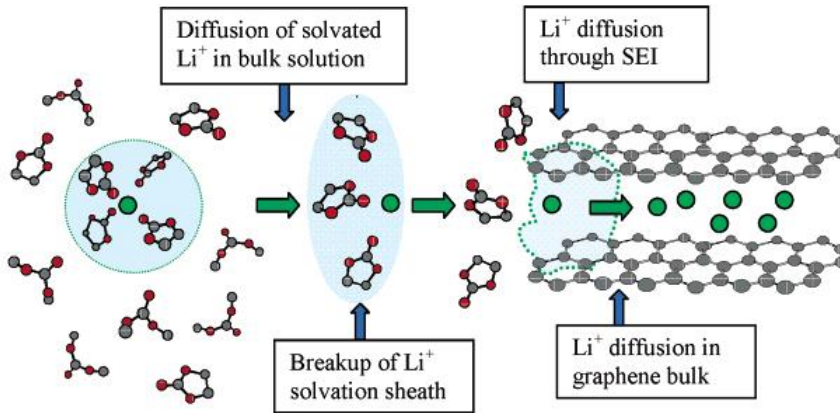


Figure 2.7: The impedance components associated with a solvated Li-ions journey from the solution bulk to the graphite interior [26].

Xu et al. [26, 27] (2007) studied the effect of the ratio of cyclic to linear carbonates on the activation energy associated with the charge transfer process. They found that the activation energy increased with an increasing ratio of EC/EMC and EC/DMC up to an EC content of 40 %. They rationalized this as an effect of the solvation sheet structure. Above 40 % the solvation sheet consists of EC molecules only. When the EC content is below 30 % fewer than three EC molecules are averagely available for each Li^+ and the linear carbonates appear in the solvation sheet. Due to their lower dielectric constant, the linear carbonates have a weaker interaction with the Li^+ than the cyclic carbonates. Hence, presence of linear carbonates in the solvation sheet would yield a lower energetic barrier associated with the Li^+ desolvation. In practical applications, the electrolytes for Li-ion batteries usually contain EC between 20 and 40 %. This ratio has been derived from repeated trial-and-error. The authors now rationalized this ratio as a compromise between effective protection and a low energetic barrier associated with Li^+ desolvation.

2.5 Degradation

Over time Li-ion batteries experience capacity loss, impedance rise and power fading upon cycling. The decrease in performance do not originate from one single cause, but from a number of processes and their interactions. Here, the main degradation mechanisms of graphite electrodes will be described. The mechanisms are presented in Figure 2.8.

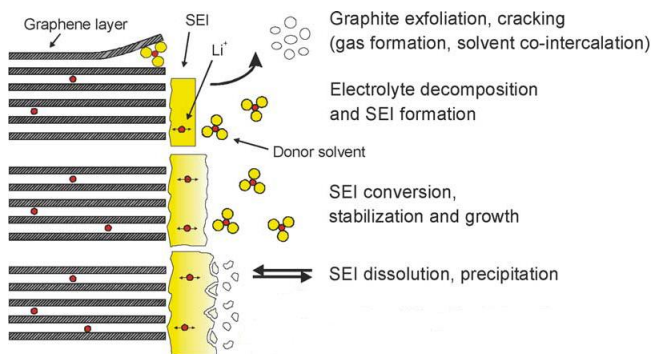


Figure 2.8: Main degradation mechanisms occurring at the graphite electrode. Modified from [7].

SEI and electrolyte

Electrolyte components with beneficial SEI formation properties should not only have a supporting effect on the SEI formation processes in the first cycles, but also on the SEI ageing processes (during prolonged cycling and storage). Normally the SEI reasonably protects the electrolyte components from further reduction, but some electrons, solvated cations, anions, solvents and impurities still seem to diffuse through the SEI-layer [7]. As a consequence, electrolyte decomposition are ongoing throughout the entire battery life, but to a lower extent and at a lower rate. This continuous SEI growth leads to capacity fade and an impedance rise. The impedance rise can be directly related to power fade.

The continuous growth of the SEI-layer might clog the micropores of the graphite electrode. The reaction products will deposit in the microporosity, and reduce the accessible active surface area of the electrode. The resultant impedance rise leads to power fade [7, 30].

Finally, the formation of acidic compounds like HF (e.g. from the reaction of LiPF_6 with trace water) has been reported to have a negative influence on the stability of the SEI [7].

Electrolyte degradation will cause an impedance rise inside the battery.

Active material

Within the bulk of the active material only minor degradation occurs [28]. The volume change related to lithiation of the graphite is approximately 10 % (Brousely2005), and the main volume change occurs during the first 20 % of lithium insertion (SOC up to ~ 20 %). The volume change might lead to micro cracks in the SEI layer, exposing the graphite surface to further SEI formation and hence capacity loss.

The strongest impact on active material changes are considered to be graphite exfoliation and graphite particle cracking due to solvent co-intercalation, electrolyte reduction inside graphite, and/or gas evolution inside graphite. These processes will lead to a rapid degradation of the electrode [7]. The graphite exfoliation results in a drastic enlargement of the surface area in contact with the electrolyte. This leads to an ongoing electrolyte decomposition on this newly formed surface. The consequence is additional charge consumption, thus increasing the irreversible capacity loss [10, 17]. In addition, the exfoliation causes graphite particles to detach from the current collector effectively making them inactive with regards to lithium storage (causing significant capacity loss).

Changes of the composite electrode

Contact loss (mechanical or electronic) within the composite electrode results in higher cell impedance. One unavoidable cause for contact loss is the volume changes of the active anode material, which may lead to mechanical disintegration within the composite electrode. The result can be contact loss between graphite particles, contact loss between current collector and graphite, contact loss between binder and graphite and contact loss between binder and current collector [7].

In addition, fluorine containing polymers like PVDF that are used as binder material react with the charged electrode to form LiF [7]. This reaction contribute to degradation in the mechanical electrode properties and to loss of lithium (capacity loss).

In summary, some of the main degradation mechanisms are listed below:

Capacity fade:

- Electrolyte decomposition (SEI formation and growth)
- Graphite exfoliation and particle cracking
- Decomposition of binder

Impedance rise:

- SEI growth/thickening of the SEI
- Clogging of micropores due to SEI growth
- Contact losses within the composite electrode
- Reduced porosity due to volume changes and SEI growth

2.6 Electrochemical stability

Electrochemical impedance spectroscopy (EIS) is an electroanalytical technique used for characterization of complicated electrode processes. EIS has been extensively used to Li-battery cells, to determine the factors limiting the performance of an electrode, including its conductivity, charge-transfer properties, properties of the SEI layer etc [31]. EIS is a fast and non-destructive technique able to identify different reaction mechanisms and possible origins of cell degradation processes [7], like the degradation processes described in the previous chapter.

The electrochemical impedance is normally measured using a perturbation AC voltage signal V with small amplitude V_A applied at a frequency f . The voltage signal $V(t)$, expressed as a function of time t , has the form of a sinusoidal wave

$$V(t) = V_A \sin(2\pi ft) = V_A \sin(\omega t) \quad (2.5)$$

If the system is linear, the response current signal $I(t)$ to the perturbation is also a sinusoidal wave with the same frequency, but with different phase (ϕ) and amplitude, I_A :

$$I(t) = I_A \sin(\omega t + \phi) \quad (2.6)$$

An expression analogous to Ohm's Law is used to calculate the complex impedance of the system as the ratio of the input voltage $V(t)$ and the output measured current $I(t)$:

$$Z = \frac{V(t)}{I(t)} = \frac{V_A \sin(\omega t)}{I_A \sin(\omega t + \phi)} \quad (2.7)$$

The impedance is a complex number,

$$Z = Z' + jZ'' \quad (2.8)$$

which depends on the properties of the investigated system [32]. The impedance is recorded for a wide range of frequencies. If the processes occurring on the cell and electrode level have different time constants, their contributions to the overall impedance may be resolved in the various frequency ranges.

For electrochemical reactions in general, the current-voltage relationship is not linear. Because of this nonlinear behaviour, the impedance has to be measured with a small amplitude V_A of the perturbation signal. Hence, only the linear part of the response is taken into account. In the general case of electrochemical kinetic studies, amplitudes of 5-10 mV are acceptable [33].

The classical approach for impedance data analysis is based on the comparison of the experimental results with an equivalent circuit model. The processes in the electrochemical cell behaves in a similar manner as simple electrical circuit components such as resistors and capacitors. The impedance of some standard circuit elements are given in Table 2.1. The impedance of the circuit may be written by applying Ohms and Kirchhoffs laws to the connection of the circuit elements.

Table 2.1: List of some standard circuit elements and their impedances.

Description	Symbol	Parameters	Impedance
Resistance	R	R	R
Capacitance	C	C	$1/j\omega C$
Inductance	L	L	$-\omega L/j$
Warburg	W	Y_0	$1/(Y_0\sqrt{j\omega})$
CPE	Q	Y_0, n	$1/(Y_0(j\omega)^n)$

Several special purpose elements have been introduced by electrochemists to model other processes. One example is diffusion in the graphite bulk, which is usually described by a Warburg element. Another example is the constant phase element (CPE), which are used when the circuit elements do not behave ideally (due to the distribution of currents and electroactive species) [32]. The CPE represents an ideal resistor when $n = 0$, a pure capacitor with a capacitance of C when $n = 1$, an inductor when $n = -1$ and a Warburg resistance when $n = 0.5$ [31, 32]. The CPE is typically applied to describe the deviation of the electrochemical impedance from an ideal capacitor.

The experimental data may be fitted to an equivalent circuit by a least square fitting procedure, based on minimizing the χ^2 , defined as the sum of the squares of the residuals.

The most common form of representation of the experimental data is the complex-plane impedance diagram (Nyquist plot). Every point corresponds to a given frequency. A typical Nyquist plot from EIS of a graphite electrode reported in the literature is shown in Figure 2.9.

Generally, two semicircles and one line is reported in the literature [34, 35]; a semicircle in the high-frequency region, another semicircle in the middle-frequency region and a Warburg-type element in the low frequency region below the potential of 0.9 V. The semicircle in the high-frequency region is related to Li-ion migration through the SEI film covered on the graphite particles, the semicircle in the middle-frequency region is attributed to charge transfer through the electrode/electrolyte interface, and the steep sloping line is assigned to solid-state diffusion of the Li-ion in the graphite matrix. The intercept with the real axis is related to frequency independent resistances, like the bulk electrolyte resistance, contact resistances and resistance across the separator(s).

Tree semicircles and one line have also been reported in the literature. Xu et

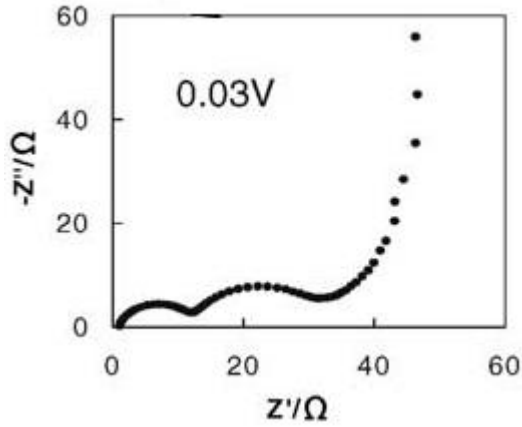


Figure 2.9: Typical Nyquist plot of a graphite anode.

al. (2011) investigated the processes of the first lithiation/delithiation of the graphite electrode by EIS. They observed three semicircles and one line in the Nyquist plots at potentials below 0.65 V; one semicircle in the high-frequency region, one semicircle in the middle-to-high-frequency region, one semicircle in the middle-to-low-frequency region and a low-frequency line. The Nyquist plot of the graphite electrode at a potential of 0.1 V during the first lithium-insertion is shown in Figure 2.10. Three semicircles and one line can clearly be seen. The equivalent circuit proposed for the analysis is also shown in the figure.

Both semicircles appearing in the middle frequency range was attributed to the charge transfer process. The authors used a theoretical model to analyse the consequence of the particle size and the nonhomogeneous distribution of the mass of porous electrodes on the electrode's impedance. The results showed that the nonhomogeneous, multilayered porous microstructure of the graphite electrode can result in three semicircles appearing in the Nyquist plots.

2.7 Thermal stability

Safety of lithium-ion batteries is mainly related to thermal reactivity of the materials in the battery. Several exothermic reactions occur inside a cell as its temperature increases. Thermal reactions at the anode can arise at temperatures

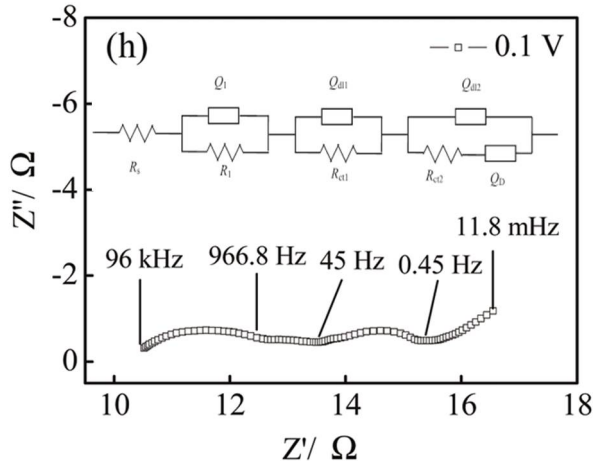


Figure 2.10: Nyquist plot of the graphite anode at a potential of 0.1 V during the first lithium-insertion and the proposed equivalent circuit [31].

below 100 °C. Heat evolution from these reactions might induce much higher heat evolution from reactions at the cathode. When the heat output exceeds the thermal diffusion, uncontrolled temperature rise occurs. This phenomenon is called thermal runaway [8, 36]. The runaway risk is induced by electrical factors (long-term cycling, high rate, overdischarge or overcharge), temperature and mechanical damage (external or internal shorts after a crash, water ingress) [37].

Effort is made to find suitable materials and electrolytes which are able to minimize the heat generation. Many studies have investigated the thermal stability of graphite anodes with electrolyte in Li-ion cells. Some of the studies are presented here. The thermal stability is usually studied by means of differential scanning calorimetry (DSC) [37], which will be described in the next section.

Yamaki et al. [36] (2002) reported in 2002 the thermal stability of natural graphite and 1M LiPF₆ 1:1 EC:DEC electrolyte. A mild heat generation was observed from 130-280 °C for the lithiated graphite in the presence of electrolyte. This exothermic response was attributed to the reaction between the electrolyte and the lithiated carbon forming new SEI. They assumed that the presence of polyvinylidene fluoride (PVDF) binder prevented SEI formation on the graphite surface covered by the binder. Upon heating the binder swells, exposing the lithiated graphite to the electrolyte, thus initiating SEI formation. At 280 °C a sharp exothermic response was observed. This peak was attributed to the breakdown of the SEI,

allowing a direct reaction of the lithiated graphite with the electrolyte.

In a recent work from 2012, Gachot et al. [37] reported the thermal behaviour of SFG6 graphite and 1M LiPF₆ in 1:1 EC:DEC electrolyte. The DSC curve of the lithiated graphite in the presence of the electrolyte displayed a broad multi-step exothermic response spanning from 120-270 C. This behaviour was assigned to the reduction of electrolyte with the lithium stored in the graphite after SEI cracking.

Verma et al. [10] claimed that there are two prime reactions occurring at elevated battery temperature. First, transformation of the SEI layer occurs. Here, the components like lithium alkyl carbonates and semicarbonates convert to the stable components like Li₂CO₃. The temperature at which this occurs is highly dependent on the salt and solvent of the electrolyte, type of carbon material and its specific surface area. For 1M LiPF₆ in ethylene carbonate (EC) and diethylcarbonate (DEC) the onset temperature was found to be 105 °C. The transformed SEI layer allows lithium from the carbon to come into contact with the electrolyte and electrons to pass through the SEI layer. Hence, at 120-140 °C, the second reaction occurs: The reaction of active material with the SEI layer, or the SEI layer with the electrolyte, or the active material with the electrolyte.

A recent study from 2011 by Haik et al. [6] reported the thermal behaviour of three commercial graphites (a carbon-coated graphite material (G5) from ConocoPhillips and two types of synthetic graphite flakes) in two different electrolyte solutions: 1M LiPF₆ in 3:7 EC:EMC and 1M LiPF₆ 1:1 EC:DMC.

The DSC curve of the pure 1M LiPF₆ 3:7 EC:EMC electrolyte solution showed an endothermic decomposition of EMC beginning near 180 °C that was followed by an exothermic decomposition of EC.

The DSC curves of cycled and fully lithiated graphites in the presence of electrolyte showed thermal responses in three temperature ranges. The observed thermal responses and their possible explanations will be presented in the following. A typical DSC curve from the study is presented in Figure 2.11.

From 80-120 °C an exothermic heat release was observed, attributed to the transformation of the SEI layer. The metastable components (lithium alkyl carbonates, lithium alkoxides) of the SEI layer decompose and react with intercalated lithium and with components of the electrolyte. The suggested reaction scheme is presented below:



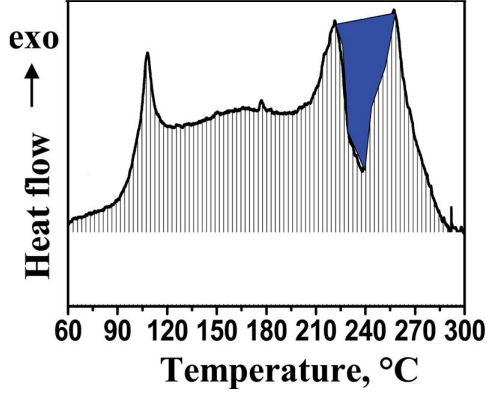
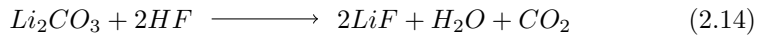
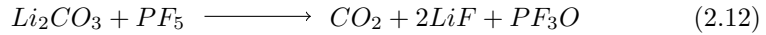
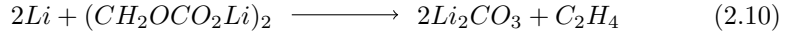


Figure 2.11: A typical DSC curve from the study by Haik et al. [6], showing the response of a cycled and fully lithiated graphite in the presence of electrolyte. Exothermic reactions are displayed as upward responses. The endothermic process is indicated with blue colour.



The first reaction (2.9) is not likely to occur, or be significant, as the SEI on the completely delithiated graphite in the presence of electrolyte did not participate

in any thermal reactions between 80 and 120 °C . Hence, the authors suggested that the presence of Li^+ is a requirement for thermal reactions.

After the complete destruction of the SEI layer the final stable surface species are LiF and possibly Li_2O . These components do not form a dense passivation protective layer on the graphite surface.

Since there no longer exist a SEI layer that can act as passivation agent, a mild exothermic response caused by continuous reactions between the lithiated graphite and the electrolyte was observed from 120-180 °C. This involves the reduction of solvent molecules on the graphite/liquid interface (i.e. forming new SEI), accompanied by the removal of Li from the graphite structure. At the same time LiPF_6 decomposes thermally to LiF and PF_5 , and the latter molecule is further involved in a variety of reactions, as seen in the proposed reaction scheme. Again, the newly formed species, LiF and Li_2O , do not provide sufficient protection of the lithiated graphite surface from interaction with the solution.

The chemical delithiation at temperatures between 80 and 180 °C leads to a reduced degree of intercalation and the stepwise decrease of stages from LiC_6 to LiC_{12} , LiC_{18} and C, as supported by XRD investigations.

Above 200 °C two larger exothermic responses separated by an endothermic response was observed. The first exothermic peak was attributed to the decomposition of the electrolyte. The thermal decomposition of the electrolyte solution involves the evolution of gaseous products like CO_2 , C_2H_4 etc.

The endothermic response was suggested to be a result of solvent co-intercalation into the graphite structure, causing graphite exfoliation. The elevated temperatures and the non efficient SEI layer facilitate thermodynamically favourable interactions between the lithium intercalated into the graphite structure and solvent molecules, spontaneously forming graphite-Li-solvent intercalation compounds. These compounds are highly reactive and decompose with gas evolution, causing a substantial increase in the pressure between the graphene layers. When the pressure exceeds some critical value, the graphite exfoliates. The authors proposed that the presence of EC in the electrolyte was important for the graphite exfoliation process. In addition, they emphasized that only Li intercalated graphite undergoes the observed exfoliation.

The last exothermic peak was believed to be a result of the exfoliation, which exposes fresh active graphite surface area to the solution species. The fresh surface and the release of Li-ions stimulate further thermal reactions of the solution species and their thermal products. At the same time, thermal decomposition of the

PVDF binder are assumed to take place.

The authors emphasised that the particle morphology and crystallographic structure play a significant role in the thermal stability of the lithiated graphite electrode. They suggested that the ratio of basal to edge planes was important for the degree of exfoliation. A large size of the basal planes on the particle surface may lead to a longer diffusion path for the gas bubbles, which can result in a build-up of a higher pressure between the graphene layers and more enhanced exfoliation. It was observed that the flaky graphites with higher basal plane area had larger morphological changes and consumed more heat than the graphite with rounder particles. The authors pointed out that the occurrence of the endothermic process may ensure a significant self cooling which may have a positive effect from a safety point of view.

In summary, several factors affect the thermal stability:

- Electrolyte composition
- Graphite structure (ratio of basal planes to edge planes)
- Surface area of the graphite
- Degree of lithiation
- Stability of the SEI layer

2.7.1 Differential scanning calorimetry

Differential scanning calorimetry is a well established measuring method which is extensively used to study the thermal stability of Li-ion batteries.

An accurate definition of differential scanning calorimetry is as follows [38]: 'Differential scanning calorimetry means the measurement of the change of the difference in the heat flow rate to the sample and to a reference sample while they are subjected to a controlled temperature program.'

Two basic types of differential scanning calorimeters are distinguished: The heat flux DSC and the power compensated DSC. In this work, the power compensated DSC were used, and hence will be the only one described. The measuring system of the power compensated DSC consists of two identical microfurnaces, one for the sample and one for a reference. During heating-up, the same heating power

is supplied to both microfurnaces in order to change their mean temperature in accordance with a pre-set heating rate (ex. 10 °C/min). When a thermal asymmetry occurs, for example when a reaction occurs in the sample, a temperature difference results between the sample and the reference. This temperature difference is compensated by an additional electrical heating power of the sample furnace, so as to keep the temperatures of the sample and reference equal. The compensation energy is equal to the heat consumed or generated by the sample.

As mentioned, the DSC is generally operated by a controlled program which changes the temperature in time. The temperature might be kept constant (isothermal mode) or changed linearly in time (scanning mode). In scanning mode the measured heat flow rate Φ is made up of three parts:

$$\Phi(T,t) = \Phi_0(T) + \Phi_{Cp}(T) + \Phi_r(T,t) \quad (2.16)$$

The first term on the right hand side is caused by an unavoidable asymmetry of the DSC. The DSC is not perfectly symmetric and the heat exchange of the sample and reference with the surroundings is somewhat different. This results in a non-zero heat flow rate even in the isothermal mode. The second term is caused by the difference in heat capacity of the sample and the reference, while the third term is the heat flow contribution from a reaction or transition occurring in the sample.

The heat flow rate is measured at regular intervals together with the temperature (or time). This raw data set establishes the DSC curve, as shown in Figure 2.12. The first term on the right hand side of the equation above defines the zeroline. This curve is measured with the instrument empty, or with empty sample containers. The first two terms together define the 'baseline', which is the heat flow rate curve produced at steady state conditions (no reactions or transitions in the sample). The third term of the equation is the 'peak' of the measured curve.

The characteristic temperatures of the DSC curve is defined as follows: T_i is the initial peak temperature, while T_e is the extrapolated peak onset temperature. These two temperatures define two different methods for finding the onset temperature of the reaction or transition which occurred in the sample. Either one can be used, as the difference between the two is smaller than the repeatability error of the measurement results. T_p is the peak maximum temperature, T_c is the extrapolated peak offset temperature and T_f is the final peak temperature.

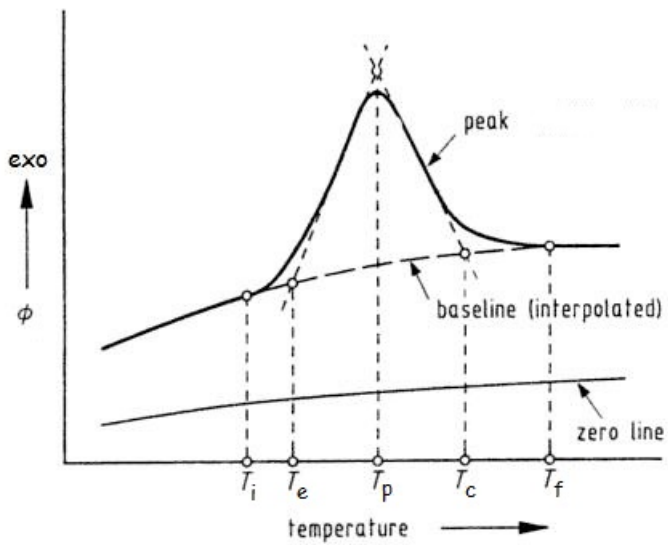


Figure 2.12: A typical measured DSC curve with some characteristic terms. Modified from [38]

Chapter 3

Experimental procedures

3.1 Materials

In this work two synthetic graphites were investigated; CPreme®G8 supplied by ConocoPhillips and A2(2650) supplied by Elkem. (2650) indicates that the material has been heat-treated to 2650 °C under N₂ atmosphere. The CPreme graphite has a uniform, homogeneous, graphite-on-graphite surface coating.

3.1.1 Particle size distribution measurements

The particle size distributions and particle sizes were measured at Elkem Carbon with a CamSizer XT from Retsch Technology. The measurements were conducted by others that have been acknowledged.

3.1.2 Scanning electron microscopy (SEM)

The graphite powders were investigated by scanning electron microscopy to reveal the surface structures and particle shapes. The powder samples were gold sputter coated with an Edwards Sputter Coater S150B. SEM pictures were recorded with a Hitachi S-3400N. The SEM was operated in secondary electron mode at 15 kV, 33% current and with working distances between 5.2 mm and 6.8 mm.

3.1.3 Nitrogen adsorption measurements

Nitrogen adsorption measurements were performed to reveal the surface characteristics of the graphites, i.e. to find the BET specific surface area and micropore area, and to estimate the relative and absolute extents of the basal plane, edge plane and defect surface areas. The measurements were performed with liquid N₂ temperature (77.3 K) using a TriStar II 3020 apparatus by Micromeritics Instrument Corporation. Before measurements the powder samples were dried and degassed at 250 °C overnight until a pressure lower than 0.15 mbar was reached. The specific surface area and the micropore area were calculated with the standard instrument software (version 1.03) in accordance with the BET method. The extents of basal planes, edge planes and defect surface areas were determined with DFT Plus software implemented in the Tristar II.

3.2 Electrochemical characterization

3.2.1 Electrode preparation

The graphite electrodes used for laboratory test cells were initially prepared by tape casting slurries onto copper foils. Slurries were prepared by mixing dry graphite powder, polyvinylidene fluoride binder (PVDF, Solvay), carbon black (Super P Li, Timcal) and N-methyl-2-pyrrolidone solvent (NMP, Sigma-Aldrich). The recipes are given in Table 3.1. The slurries were ball milled with a Retch PM 100 planetary mill for two hours to produce homogeneous mixtures.

Table 3.1: Slurry recipes for electrode preparation.

Material	Graphite [wt%]	Carbon black [wt%]	PVDF [wt%]	NMP [wt%]
CPreme G8	34.44	1.17	2.69	61.70
Elkem A2 (2650)	36.59	0.95	2.04	60.42

The slurry was tape casted onto a copper foil (Circuitfoil, ~ 10 μm thickness) current collector using the doctor-blade technique. The gap of the doctor blade was set to 150 μm . The wet film was dried on the tape cast bed at a temperature of 60 °C for two hours.

The electrode sheets were transferred into a Binder Vacuum Drying Furnace VD 23 and dried at 120 °C overnight under vacuum. A further drying step was done

in a MBRAUN UNIlab glove box attached oven under vacuum at 80 °C for two hours. Thereafter, the electrode sheets were stored in the argon filled glove box (MBRAUN UNIlab). The final weight ratios of the electrode components are given in Table 3.2. The average mass loadings of the CPreme G8 cast and the Elkem A2 (2650) cast are 5.9 ± 0.4 mg/cm² and 3.8 ± 0.2 mg/cm², respectively.

Table 3.2: Final weight ratios of the electrode components.

Material	Graphite [wt%]	Carbon black [wt%]	PVDF [wt%]
CPreme G8	90.11	2.93	6.96
Elkem A2 (2650)	92.50	2.35	5.15

3.2.2 Electrolyte preparation

Two different electrolyte compositions were prepared and used for this work. The electrolytes were prepared by others that has been acknowledged. The electrolytes consisted of the organic solvents ethylene carbonate (EC, anhydrous 99 %, Sigma-Aldrich), dimethyl carbonate (DMC, anhydrous ≥ 99 %, Sigma-Aldrich) and ethyl methyl carbonate (EMC, ≥ 99.0 %, Merck KGaA) and lithium hexafluorophosphate (LiPF₆, battery grade ≥ 99.99 %, Aldrich). The electrolytes were made under argon atmosphere. The salt was dried in a MBRAUN UNIlab glove box attached oven under vacuum at 80 °C before mixing. The electrolyte compositions and their abbreviations (that are used throughout this text) are given in Table 3.3. The difference between the two electrolytes is the relative amounts of EC, DMC and EMC.

Table 3.3: Compositions (weight based ratios) and abbreviations for the electrolytes used in this work.

Electrolyte composition	Abbreviation
1:2:2 EC:DMC:EMC + 0.9M LiPF ₆	E1
4:3:3 EC:DMC:EMC + 0.9M LiPF ₆	E2

3.2.3 Cell assembly

The charge/discharge performance of the graphites were evaluated with the help of small lithium/graphite laboratory test cells (coin cells/half cells). In these

laboratory test cells, graphite is the cathode and metallic lithium is used both as the counter electrode and the reference electrode. Hence, the potential is reported with respect to a Li/Li^+ reference system. For a practical battery system, the Li/Li^+ electrode is replaced by the actual cathode material. Lithium intercalation is thus referred to as the charge process, and lithium deintercalation as the discharge process.

A schematic illustration of the internal design of a coin cell is provided in Figure 3.1.

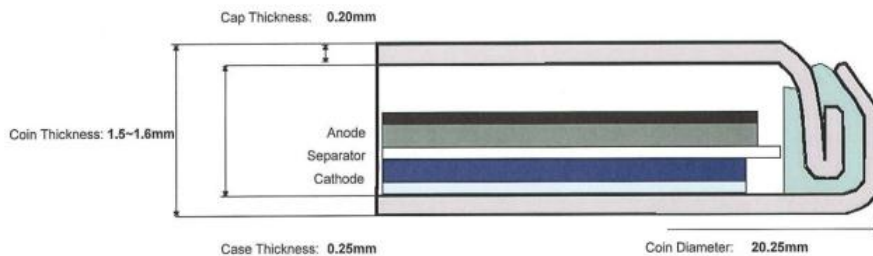


Figure 3.1: Schematic illustration of a coin cell [39].

The coin cell consists of a bottom case, the graphite electrode (cathode), separator, lithium counter electrode (anode), a spacer to fill the free space inside the coin cell and a cap on top. The cell is hermetically sealed with a plastic gasket. The case, cap and spacer were provided by Hohsen corp. and are made of stainless steel (SUS316L alloy). The coin cell is 1.6 mm thick and has a diameter of 20.25 mm (CR2016 Hohsen coin cell).

The coin cells were assembled in an argon-filled glove box (MBRAUN UNILab) with water and oxygen contents below 0.1 ppm. A plastic gasket was placed in the bottom case of the CR2016 coin cell from Hohsen corp. Graphite electrodes of diameter 16.0 mm were cut from the electrode sheets and weighed on a scale provided by Mettler Toledo. The thickness was measured, and the electrode was placed in the bottom case of the coin cell. A 16.0 mm microporous ion-conductive separator sheet (Celgard 2320) of 20 μm thickness was placed between the graphite electrode and the 14.0 mm diameter counter electrode cut from 0.75 mm thick lithium foil (99.9 %, Alfa Aesar). The lithium was brushed prior to mounting to remove surface films. 15 μl electrolyte was applied to each side of the separator, in total 30 μl of electrolyte, sufficient to soak the graphite electrode and the separator. A 16.0 mm diameter stainless steel (SUS316L alloy) spacer of 0.3

mm thickness was placed on top of the lithium electrode to fill the free space inside the coin cell. Finally, the battery cap was placed on top. The cells were hermetically sealed in an automatic crimping machine provided by Hohsen Corp. A photograph of the cell components is provided in Figure 3.2. Cells with an open circuit potential lower than 2.0 V were abandoned.

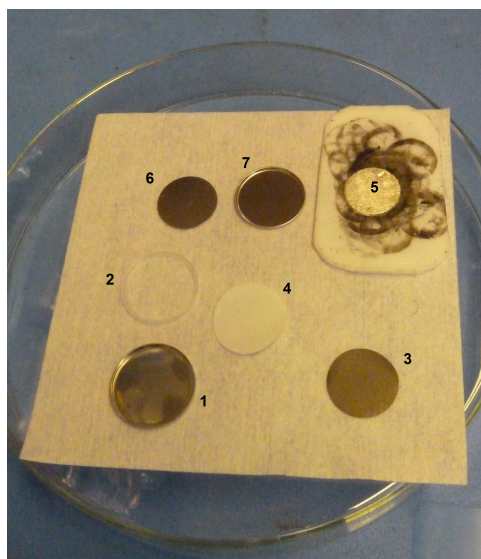


Figure 3.2: Cell components in order of assembly: 1.bottom, 2.gasket, 3.graphite electrode, 4.separator, 5.lithium counter electrode, 6.spacer and 7.top.

A three electrode cell was assembled for electrochemical impedance spectroscopy of the CPreme G8 graphite with the E2 electrolyte. A schematic illustration of the internal design of the three electrode cell is provided in Figure 3.3.

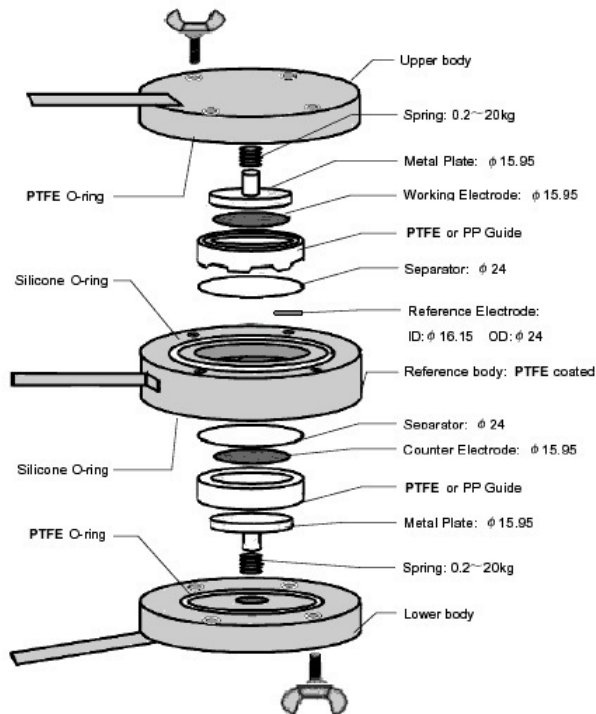


Figure 3.3: Schematic illustration of a three electrode cell [40].

The three electrode cell was assembled in an argon-filled glove box (MBRAUN UNILab) with water and oxygen contents below 0.1 ppm. A 14.0 mm diameter counter electrode was cut from a 0.75 mm thick lithium foil (99.9%, Alfa Aesar) and placed in the lower body of a HS-3E test cell from Hohsen Corp. The lithium was brushed prior to mounting to remove surface films. A 16.0 mm microporous ion-conductive polypropylene separator sheet (Celgard 2320) of 20 μm thickness was placed between the graphite electrode and a reference electrode. The reference electrode was a 1 mm x 1 mm x 4 mm piece of lithium placed in the circumference of the separator, touching the inner wall of the reference body. A 20 mm separator sheet (Celgard 2320) was placed on top of the reference. 60 μl electrolyte was applied to ensure that the graphite electrode and the separators would be sufficiently soaked. A graphite electrodes of diameter 16.0 mm were cut from the electrode sheets. The weight and thickness of the graphite electrode was measured. The graphite electrode was placed on top of the separator with the

copper foil side facing up. The upper body was placed on top and the cell was sealed with eight screws.

Tape was put in the gap between the lower body and the reference body and between the upper body and the reference body while the cell was inside the glove box, to ensure that no oxygen or moisture would enter the inner parts of the cell after removing it from the glove box.

3.2.4 Electrochemical cycling

Charge/discharge cycling was carried out using two different computer controlled potentiostats: A Bio-Logic VMP3 (Versatile Multichannel Potentiostat) multichannel potentiostat/galvanostat with EC-lab[®] software and a Solartron Analytical 1480 MultiStat multichannel potentiostat/galvanostat with CellTest[®] software.

Varying charge/discharge rates (C-rates) were used for the cycling of the test cells. A current density of 1C is defined as the current required to completely charge or discharge an ideal cell with theoretical capacity (372 mAh/g) in one hour. A relatively low current density of 10 mA/g (C/37) was chosen in the first Li⁺ intercalation cycle. This rate was chosen to ensure that the SEI formation was as effective as possible. A current density of 46.5 mA/g (C/8) was chosen for the next five cycles, in order to ensure the formation of a mature SEI layer. In the subsequent cycles different C-rates were employed in order to examine the performance of the cells. Each coin cell was cycled for 52 cycles, with one of the two different cycling methods used in this work:

Rapid cycling:

1. Galvanostatic discharge at 10 mA/g (C/37) until a cut-off potential of 5 mV vs. Li/Li⁺.
2. Discharging continued potentiostatically at 5 mV until the current dropped below 5 mA/g.
3. Galvanostatic charge at 10 mA/g until 1.5 V vs Li/Li⁺.
4. Five cycles between 1.5 V and 5 mV at a rate of C/8.
5. 45 cycles between 1.5 V and 5 mV at a rate of C/2.
6. One cycle between 1.5 V and 5 mV at a rate of C/37.

Moderate cycling:

1. Galvanostatic discharge at 10 mA/g (C/37) until a cut-off potential of 5 mV vs. Li/Li⁺.

2. Discharging continued potentiostatically at 5 mV until the current dropped below 5 mA/g.
3. Galvanostatic charge at 10 mA/g until 1.5 V vs Li/Li⁺.
4. 16 cycles between 1.5 V and 5 mV at a rate of C/8.
5. Two cycles between 1.5 V and 5 mV at a rate of C/37.
6. Two cycles between 1.5 V and 5 mV at a rate of C/8.
7. Two cycles between 1.5 V and 5 mV at a rate of C/4.
8. Two cycles between 1.5 V and 5 mV at a rate of C/2.
9. Two cycles between 1.5 V and 5 mV at a rate of C/37.
10. 24 cycles between 1.5 V and 5 mV at a rate of C/8.
11. One cycle between 1.5 V and 5 mV at a rate of C/37.

From the end of step three in the above cycling methods each charging continued potentiostatically at 1.5 V for ten seconds followed by a ten seconds relax step, while the discharging continued potentiostatically at 5 mV for two minutes followed by a two minutes relax step.

A matrix of cell combinations (graphite material, electrolyte and cycling method) are given in Table 3.4. Three test cells were cycled per combination. All tests were carried out at room temperature.

Table 3.4: Matrix of cell combinations.

Material	Rapid cycling	Moderate cycling
CPreme G8	E1, E2	E1, E2
Elkem A2 (2650)		E2

3.2.5 Scanning electron microscopy of electrodes

Pristine and cycled graphite electrodes were investigated in order to discover any difference in the morphology after the cycling. SEM pictures were recorded with a Hitachi S-3400N. The SEM was operated in secondary electron mode at 5 kV (electrodes), 33% current and with working distances between 5.2 mm and 6.8 mm.

3.2.6 Electrochemical impedance spectroscopy

As previously mentioned, one test cell was made for electrochemical impedance spectroscopy. The cell was initially cycled at a relatively low current density of 10 mA/g (C/37) to ensure that the SEI formation was as effective as possible. A current density of 46.5 mA/g (C/8) was chosen for the next five cycles, in order to ensure formation of a mature SEI layer. The cycling was performed with a Bio-Logic VMP3 (Versatile Multichannel Potentiostat) multichannel potentiostat/galvanostat controlled by EC-lab[®] software. The EIS were measured at two different voltages (0.90 V and 0.12 V) using a ZAHNER-Elektrik[®] IM6e potentiostat controlled by Thales Z.2.10 software. The experiments were performed in the following manner:

1. Galvanostatic discharge at 10 mA/g (C/37) until a cut-off potential of 5 mV vs. Li/Li⁺.
2. Charging continued potentiostatically at 5 mV until the current dropped below 5 mA/g.
3. Galvanostatic charge at 10 mA/g until 1.5 V vs Li/Li⁺.
4. Five cycles between 1.5 V and 5 mV at a rate of C/8.
5. Galvanostatic discharge until 0.9 V at a rate of C/8.
6. Electrochemical impedance spectroscopy potentiostatically measured at 0.90 V.
7. Galvanostatic discharge from 0.90 V to 0.12 V at a rate of C/8.
8. Electrochemical impedance spectroscopy potentiostatically measured at 0.12 V.
9. Galvanostatic discharge at a rate of C/8 until 5 mV.
10. Galvanostatic charge at rate of C/8 until 1.5 V.
11. Nine cycles between 1.5 V and 5 mV at a rate of C/8.
12. Repetition of steps 5. to 9.

The EIS were measured with an AC oscillation of 10 mV amplitude over the frequency range from 10 mHz to 1.0 MHz. The measurements were performed after the current reached a value of less than 10 μ A, in order to attain steady-state conditions. Three spectra were recorded and averaged. All tests were performed at room temperature.

The experimental data were analysed with ZSimpWin Electrochemical Impedance Spectroscopy Analysis Software, version 3.21.

3.3 Thermal analysis

High temperature DSC analysis of the graphite electrodes soaked with fresh electrolyte was performed in order to reveal the thermal stability of the electrodes for the various combinations of graphite materials, electrolytes and cycling methods. In addition, analysis of pure electrolytes were performed.

3.3.1 DSC sample preparation

Before the thermal analysis the cells were discharged at a rate of 10 mA/g (C/37) until 5 mV. Discharging continued potentiostatically at 5 mV until a current of 5 mA/g was reached to ensure homogeneity of the electrodes.

The DSC samples were assembled inside an argon-filled glove box to prevent the SEI layer and the electrolyte from chemically decomposing. The cycled cells were disassembled with a coin cell disassembling tool from Hohsen Corp. Samples of diameter 4.0 mm were punched out from the graphite electrodes. The samples were weighed on a scale provided by Mettler Toledo. Some samples contained the Cu-foil, while others did not, as the Cu-foil fell off some of the samples. Typical weight of the samples were 2.0 mg (with Cu-foil) and 1.0 mg (without Cu-foil).

The samples were placed inside high pressure stainless steel capsules, specified to withstand an internal pressure of 150 atmospheres, provided by PerkinElmer. The capsules had an effective volume of 30 μl . Fresh electrolyte, similar to the one used in the cell, was also added to the capsules. The graphite/electrolyte ratio was approximately 1:3. A gold-plated copper seal was placed on top of the capsule bottom, under the capsule top. The capsules were then hermetically sealed with a sealing tool provided by PerkinElmer. In order to determine the homogeneity of the electrode and the reproducibility of the analysis, three samples were cut and analysed from each electrode. The samples with pure electrolytes were made in a similar manner. 3.5 μl fresh electrolyte were added to the capsules, which were hermetically sealed. Two samples of each electrolyte were analysed, in order to ensure reproducibility of the analysis.

The equipment used for the DSC sample preparation are shown in Figure 3.4.

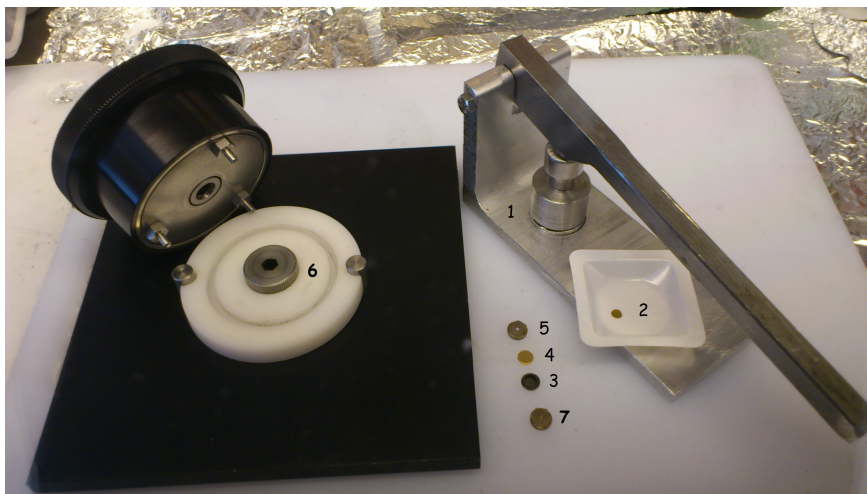


Figure 3.4: Equipment used for the DSC sample preparation. 1.Punching tool, 2.Sample, 3. Capsule bottom, 4.Seal, 5.Capsule top, 6.Sealing tool and 7.Mounted sample. Note that lithiated graphite is gold coloured.

3.3.2 DSC analysis

The DSC measurements were carried out using a PerkinElmer DSC 7 apparatus with a PerkinElmer thermal analysis controller TAC 7/DX. The hardware was controlled by Pyris software version 3.81. The weight of each capsule (with sample) was measured before and after the experiment to ensure that the system was hermetically sealed. The weight was constant in all cases, indicating that there were no leaks during the experiments. The analyses were carried out over a temperature range from 30.0 to 300.0 °C with a constant heating rate of 2.5 °C/min. The DSC analyses were conducted using an empty sample capsule as reference. The DSC curves were obtained by subtracting the background scan. As the thermal processes in the selected temperature range are found to be irreversible [6], the background scan was obtained by scanning the sample a second time right after the first scan.

The sample chamber in the PerkinElmer DSC 7 apparatus is shown in Figure 3.5.

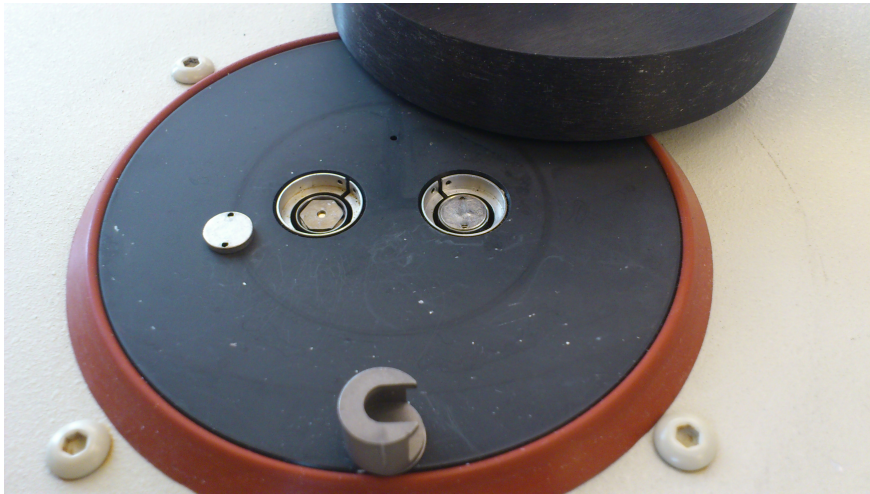


Figure 3.5: Sample chamber in the PerkinElmer DSC 7 apparatus. The crucible for the sample is to the left, while the crucible for the reference is to the right.

Chapter 4

Results

4.1 Material characterization

In this section results from the basic characterization of the graphite powders are presented. These include SEM investigations, particle size distribution measurements, and nitrogen adsorption measurements. The results will be used as a foundation for the later discussion of the electrochemical performance and thermal stability of the graphites.

4.1.1 SEM

SEM pictures of the graphite powders are shown in Fig 4.1. CPreme G8 has a potatoshaped morphology, with elongated round particles and a smooth surface. Elkem A2 (2650) has a more flaky morphology, with rougher edges and surfaces. From the SEM pictures the particle sizes seem to be similar for both graphites.

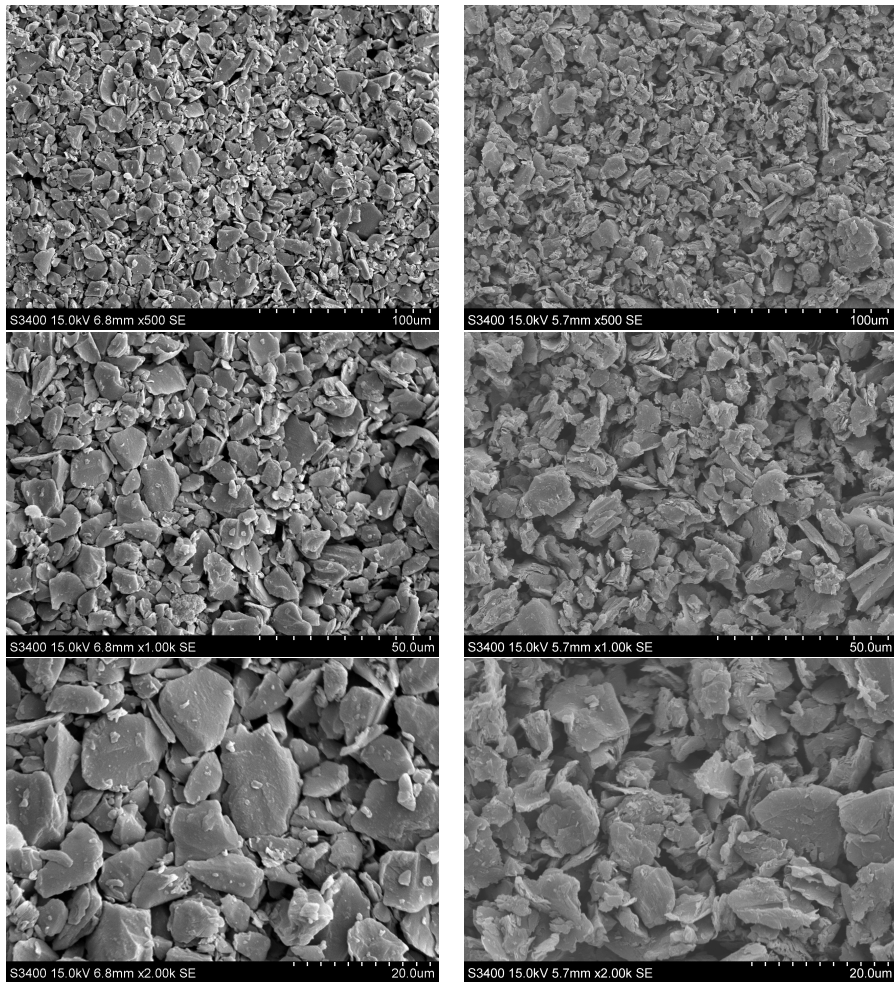


Figure 4.1: SEM pictures of the graphite powders. CPreme G8 to the left and Elkem A2 (2650) to the right.

4.1.2 Particle size distribution measurements

The particle size distribution (PDS) parameters of the graphite powders are given in Table 4.1. $d_{10\%}$, $d_{50\%}$ and $d_{90\%}$ indicates that 10 volume%, 50 volume% and

90 volume%, respectively, of the particles are smaller than the given diameters in the table.

Table 4.1: Particle size distribution parameters.

Material	$d_{10\%}$ [μm]	$d_{50\%}$ [μm]	$d_{90\%}$ [μm]
CPreme G8	5.3	8.8	14.6
Elkem A2 (2650)	5.9	11.1	20.4

From Table 4.1 it is clear that the CPreme G8 graphite powder contains smaller particles than the Elkem A2 (2650) graphite powder. In addition, CPreme G8 has a slightly more narrow particle size distribution than Elkem A2 (2650).

4.1.3 Nitrogen adsorption measurements

Surface characteristics from nitrogen adsorption experiments are provided in Table 4.2. The BET specific surface area and the BET micropore area are evaluated from BET theory. The BET micropore area corresponds to the area inside pores of diameter < 2 nm. The other properties in Table 4.2 are evaluated from density functional theory models, as described in chapter 2.2.2. Figure 4.2 shows the incremental surface area as a function of adsorptive potentials for the graphite materials. The adsorptive potential distribution centred between 50 and 60 K is ascribed to the basal plane surfaces, in accordance with literature [25]. Edge surfaces have adsorptive potentials lower than 50 K, while defect surfaces have adsorptive potentials higher than 60 K.

Table 4.2: Surface characteristics of the studied graphites.

Surface properties	CPreme G8	Elkem A2 (2650)
BET specific surface area [m^2/g]	1.79 ± 0.03	9.7 ± 0.1
BET micropore area [m^2/g]	0.17	0.46
DFT surface area [m^2/g]	1.88	11.07
Basal plane surface area [m^2/g]	1.53	6.77
Edge plane surface area [m^2/g]	0.35	2.43
Defect surface area [m^2/g]	0	1.87
Ratio of basal:edge:defect area [%]	82:19:0	61:22:17
Ratio of basal:non-basal areas [%]	82:19	61:39

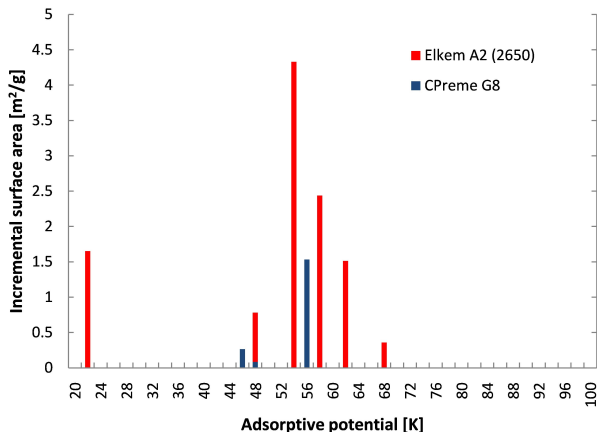


Figure 4.2: Incremental surface area vs. adsorptive potential plots of the graphites.

Nitrogen adsorption measurements revealed interesting differences between the materials. Even though the particle sizes/particle size distributions are similar, Elkem A2 (2650) has a BET specific surface area which is more than five times larger than CPreme G8. Basal planes is the prevalent surface type on both graphites, and the relative extent of edge planes is approximately equal ($\sim 20\%$ edge planes). The ratio of basal planes to non-basal planes is considerably higher for CPreme G8 than Elkem A2 (2650) (82 % versus 61 %), due to the absence of defects in CPreme G8. Elkem A2 (2650) has approx. 17 % of the surface made up of defects.

4.2 Electrochemical measurements

In this section results from the electrochemical cycling will be presented. The electrochemical cycling was performed in order to evaluate long term stability of the various combinations of graphite and electrolyte. The influence of the electrolyte is evaluated by comparing the performance of CPreme G8 with electrolytes E1 and E2. These two systems was subjected to two different cycling methods (rapid and moderate) to investigate the influence of cycling rate. The influence of the graphite structure on the performance was investigated by comparing the performance of

CPreme G8 and Elkem A2 (2650) together with electrolyte E2.

For each parameter combination three parallel test cells were assembled and cycled. The graphite loadings, thicknesses and porosities of the electrodes used for the coin cells are given in Table 4.3. The CPreme G8 samples have an average thickness of $75 \pm 3 \mu\text{m}$ and an average graphite loading of $5.91 \pm 0.41 \text{ mg/cm}^2$. The Elkem A2 (2650) samples have an average thickness of $65 \pm 2 \mu\text{m}$ and an average graphite loading of $3.77 \pm 0.20 \text{ mg/cm}^2$. It should be noted that Elkem A2 (2650) has a higher average porosity than CPreme G8 ($74.0 \pm 0.6 \%$ versus $65.2 \pm 1.5 \%$).

Table 4.3: Summary of graphite loadings, thicknesses and porosities of the electrodes used for coin cells.

Material	Sample number	Electrolyte	Cycling	Thickness [μm]	Graphite loading [mg/cm^2]	Porosity [%]
CPreme G8	1	E1	Rapid	81	6.43	64.5
CPreme G8	2	E1	Rapid	71	5.57	65.0
CPreme G8	3	E1	Rapid	74	6.14	63.0
CPreme G8	1	E1	Moderate	73	5.90	63.9
CPreme G8	2	E1	Moderate	75	6.03	64.1
CPreme G8	3	E1	Moderate	72	4.99	69.1
CPreme G8	1	E2	Rapid	78	6.1	64.6
CPreme G8	2	E2	Rapid	74	5.47	67.0
CPreme G8	3	E2	Rapid	80	6.32	64.7
CPreme G8	1	E2	Moderate	74	5.62	66.1
CPreme G8	2	E2	Moderate	81	6.38	64.8
CPreme G8	3	E2	Moderate	76	5.88	65.4
Elkem A2 (2650)	1	E2	Moderate	62	3.52	74.7
Elkem A2 (2650)	2	E2	Moderate	67	4.01	73.3
Elkem A2 (2650)	3	E2	Moderate	65	3.80	73.9

The results of the long-term cycling are shown in Figure 4.3 to Figure 4.7, where the discharge capacities are plotted against the cycle number. Figure 4.3 and Figure 4.4 show rapid cycling of CPreme G8 with electrolyte E1 and E2, respectively. The initial capacity is just above 300 mAh/g for all six samples, measured at a rate of C/37. The capacity is reduced when the rate is increased to C/8. When the rate is increased to C/2, the capacity is further reduced, until a point where the capacity starts to increase. For CPreme G8 with electrolyte E1 the capacity reaches its lowest point at ~ 10 th cycle. Subsequent cycles show a steadily increasing capacity, before the capacity reaches a maximum and start to decrease slowly. Sample 2 and 3 have a considerably higher capacity than sample 1. For the samples made with CPreme G8 and electrolyte E2 the capacity reaches

its lowest point at different cycle numbers (around cycle number 20). In contrast to the samples made with CPreme G8 and electrolyte E1, these samples show a rapid increase in capacity; the capacity is increased considerably during one cycle. After the increase the capacity is stabilized, as opposed to the samples made with electrolyte E1. The samples in Figure 4.3 and Figure 4.4 retain most of their capacities when the cycling rate is decreased to C/37 at the 52nd cycle.

Figure 4.5 and Figure 4.6 show moderate cycling of CPreme G8 with electrolyte E1 and E2, respectively, while Figure 4.7 shows moderate cycling of Elkem A2 (2650) with electrolyte E2. These figures show similar features. The capacity is reduced when the cycling rate is increased, but recovered again when the rate is decreased. Over time, the capacity is reduced when the cells are cycled at a steady rate. Sample 3 of moderate cycled CPreme G8 with electrolyte E1 shows better performance than sample 1 and 2. Elkem A2 (2650) has the highest porosity of the graphite materials and the best capacity at a rate of C/2 as compared to the other moderate cycled samples.

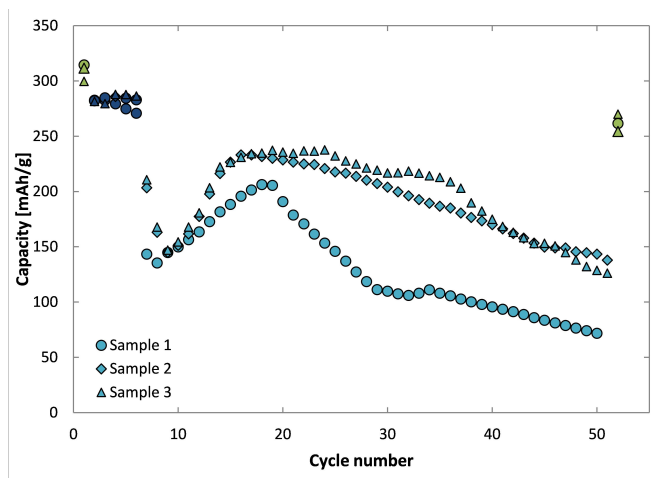


Figure 4.3: Long-term rapid cycling of CPreme G8 with electrolyte E1. The colours indicate different C-rates: Green = C/37, dark blue = C/8 and light blue = C/2.

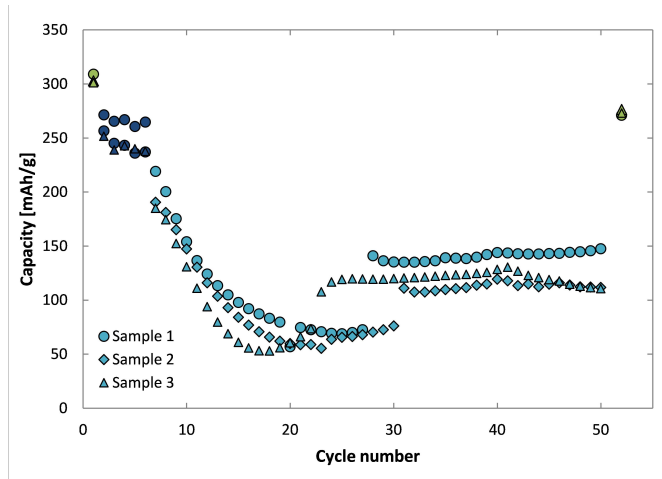


Figure 4.4: Long-term rapid cycling of CPreme G8 with electrolyte E2. The colours indicate different C-rates: Green = C/37, dark blue = C/8 and light blue = C/2.

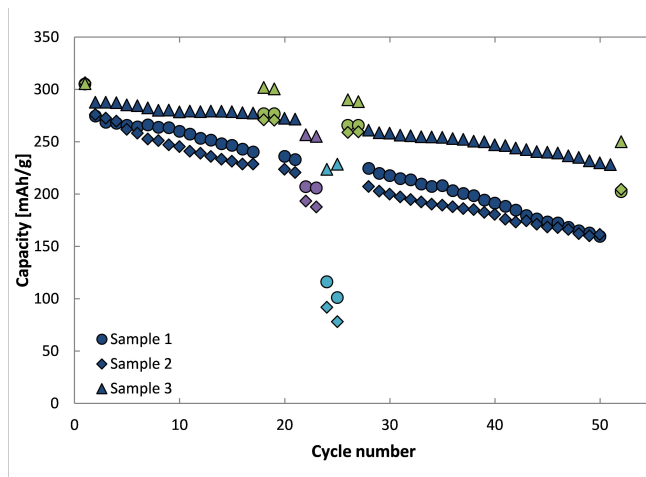


Figure 4.5: Long-term moderate cycling of CPreme G8 with electrolyte E1. The colours indicate different C-rates: Green = C/37, dark blue = C/8, purple = C/4 and light blue = C/2.

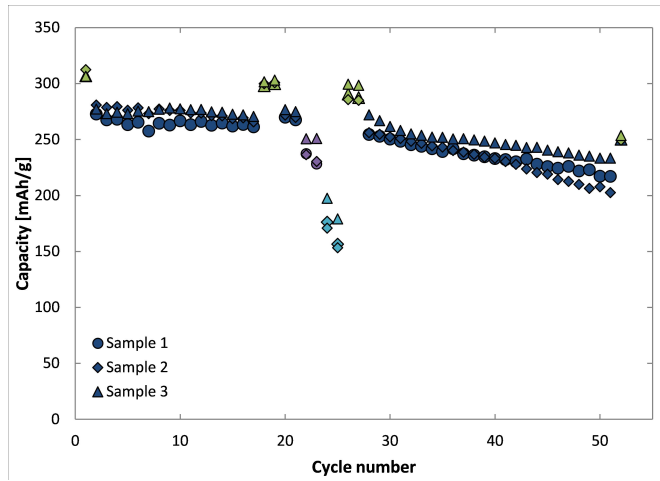


Figure 4.6: Long-term moderate cycling of CPreme G8 with electrolyte E2. The colours indicate different C-rates: Green = C/37, dark blue = C/8, purple = C/4 and light blue = C/2.

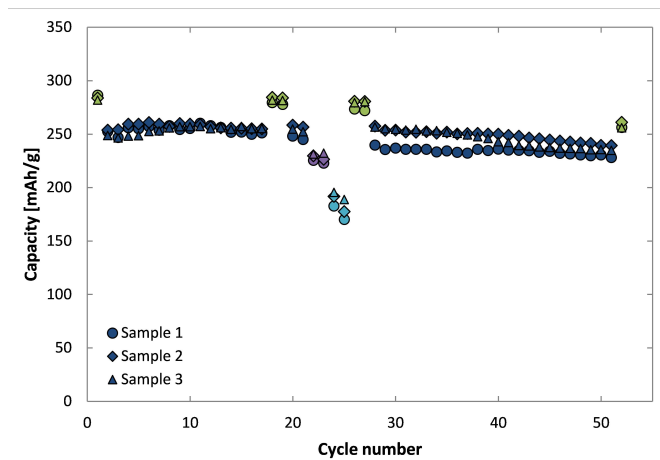


Figure 4.7: Long-term moderate cycling of Elkem A2 (2650) with electrolyte E2. The colours indicate different C-rates: Green = C/37, dark blue = C/8, purple = C/4 and light blue = C/2.

The irreversible capacity loss (ICL) is a measure of the capacity lost due to SEI formation. Most of the SEI formation occurs in the initial cycle, hence the ICL (in %) of the materials are calculated by the following formula:

$$ICL = \frac{Q_{charge} - Q_{discharge}}{Q_{charge}} \times 100 \quad (4.1)$$

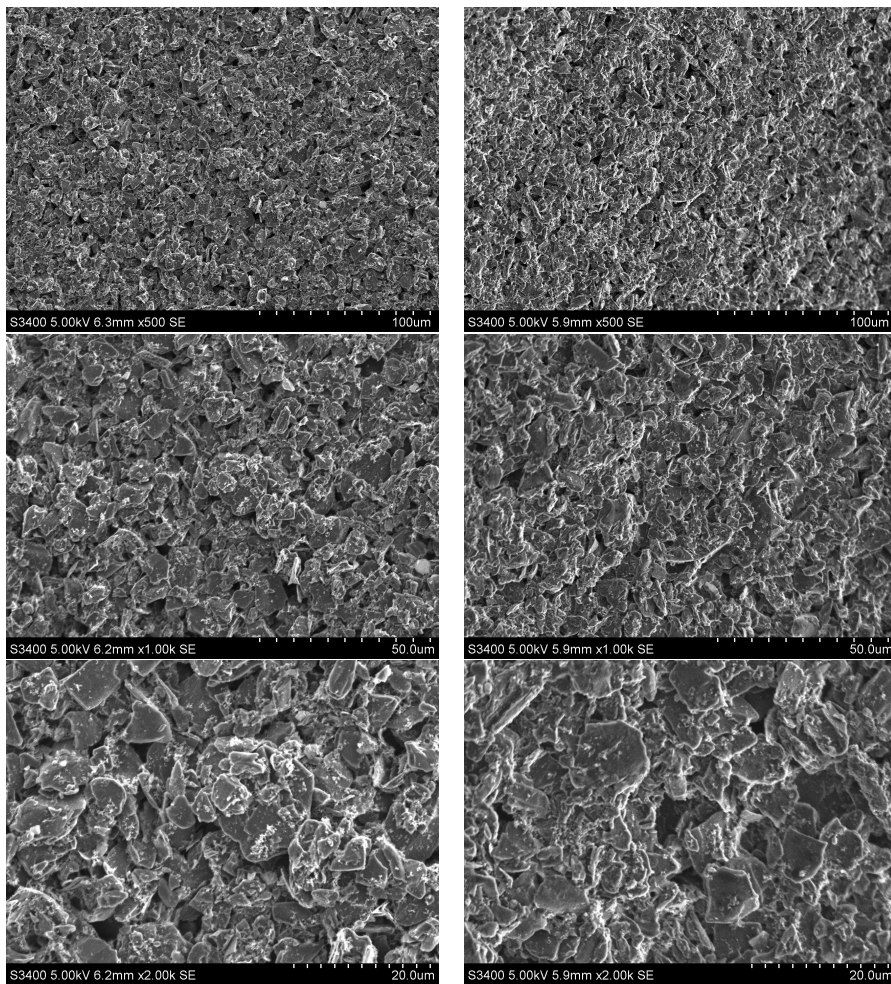
where Q_{charge} is the specific charge of the first Li^+ intercalation, and $Q_{discharge}$ the reversible specific charge of the following Li^+ de-intercalation. The performance characteristics of the graphite materials are given in Table 4.4. The values were obtained by applying a current of 10 mAh/g, corresponding to a rate of C/37, in the first and the 52. cycle. The values are averages of three test cells. All capacities are expressed per gram of active material.

Table 4.4: Performance characteristics.

Material	Electrolyte	Cycling method	ICL [%]	Reversible capacity, 1st cycle [mAh/g]	Reversible capacity, 52. cycle [mAh/g]	Retained capacity [%]
CPreme G8	E1	Rapid	7.7 ± 1.0	308.6 ± 6.4	261.9 ± 6.4	85.0 ± 3.7
CPreme G8	E1	Moderate	9.4 ± 0.4	305.7 ± 0.5	219.0 ± 22.0	71.7 ± 7.2
CPreme G8	E2	Rapid	10.3 ± 0.3	304.4 ± 3.4	273.5 ± 2.2	89.9 ± 1.6
CPreme G8	E2	Moderate	9.7 ± 0.4	308.7 ± 2.7	251.1 ± 1.8	81.4 ± 1.2
Elkem A2 (2650)	E2	Moderate	22.6 ± 2.5	284.1 ± 1.9	257.8 ± 2.3	90.7 ± 1.0

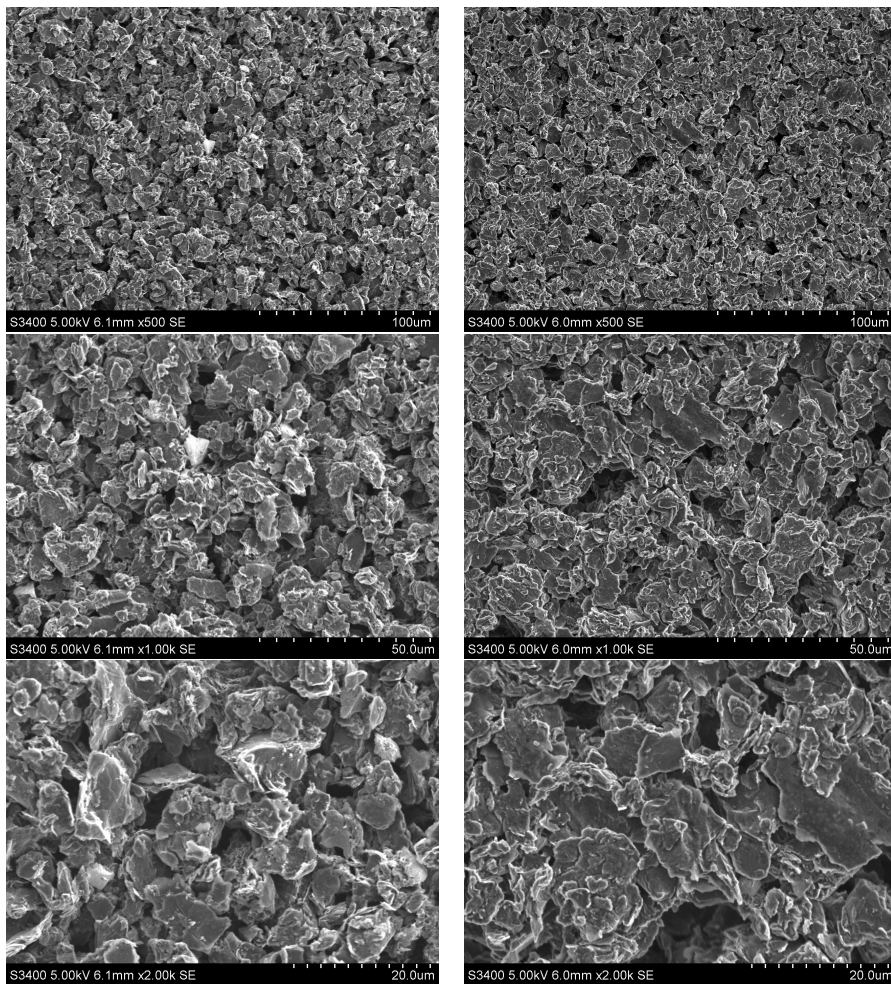
It is evident from Table 4.4 that Elkem A2 (2650) has the highest ICL of the investigated graphites. There is a tendency to a lower ICL for CPreme G8 with electrolyte E1 than for CPreme G8 with electrolyte E2. CPreme G8 have higher reversible capacity of the 1st cycle than Elkem A2 (2650). The retained capacity is higher for the rapid cycled CPreme G8 samples compared to the moderate cycled samples. For samples cycled with the same cycling method (rapid or moderate) the samples cycled with electrolyte E2 have a higher retained capacity than the samples cycled with electrolyte E1. Elkem A2 (2650) has the lowest initial capacity, but the best long-term stability, with a retained capacity on the 52nd cycle of 90.7 %.

Pristine and cycled graphite electrodes were investigated by SEM to reveal possible cracks in the particle surfaces. SEM pictures of pristine and moderate cycled CPreme G8 electrodes are shown in Figure 4.2. The other CPreme G8 electrodes showed similar features, regardless of the cycling method or electrode used. Hence, SEM pictures of only one electrode is shown.



SEM pictures of the pristine (left) and moderate cycled (right) CPreme G8 electrodes. Electrolyte E2 was used for the cycling.

SEM pictures of pristine and moderate cycled Elkem A2 (2650) electrodes are shown in Figure 4.2



SEM pictures of the pristine (left) and moderate cycled (right) Elkem A2 (2650) electrodes

A higher magnification than those shown in the figures were used during the investigation. No cracks in the particle surfaces could be seen.

4.3 Electrochemical impedance spectroscopy

In this section results from the electrochemical impedance spectroscopy will be presented. The EIS were performed in order to provide information about the electrode processes and to identify possible degradation mechanisms during cycling. CPreme G8 with electrolyte E2 was chosen for the experiments. The experiments were performed with the three electrode cell. Impedance spectra were recorded at two potentials, 0.90 V and 0.12 V during the 7th and 17th cycles. The 7th cycle was chosen in order to ensure a mature SEI layer. The potentials corresponds to a state of charge (SOC) of $\sim 0.35\%$ (almost empty) and $\sim 22\%$ (partially lithiated), respectively. The SOC was calculated based on the reversible capacity of the 1st cycle. The graphite loading, thickness and porosity of the electrode used for the three electrode cell are given in Table 4.5.

Table 4.5: Graphite loading and thickness of the electrode used for the three electrode cell.

Material	Electrolyte	Thickness [μm]	Graphite loading [mg/cm^2]	Porosity [%]
CPreme G8	E2	77	5.64	67.3

The results of the cycling are shown in Figure 4.8.

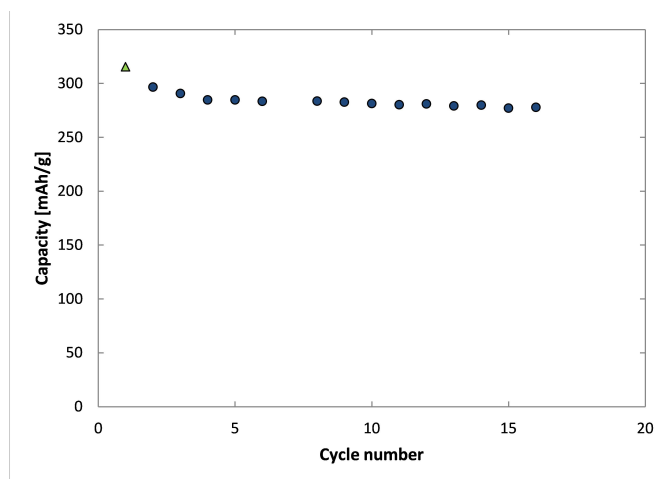


Figure 4.8: Moderate cycling of CPreme G8 with electrolyte E2 with the three electrode cell. The green symbol indicates a rate of $C/37$, while the dark blue symbols indicates a rate of $C/8$.

Figure 4.9 shows Nyquist plots of the graphite electrode at potentials of 0.90 V and 0.12 V during the 7th lithiation (7. cycle) of the cell. Three spectra were recorded and averaged for each voltage. The Nyquist plots consist of four parts; one semicircle in the high-frequency region, two semicircles in the middle-frequency region and a steep line in the low-frequency region. According to literature, as described in chapter 2.6, the semicircle in the high-frequency region can be attributed to Li-ion migration through the SEI film covered on the graphite particles. The semicircles in the middle-frequency region might both be related to the charge transfer through the electrode/electrolyte interface. The sloping line in the low-frequency region is generally attributed to solid-state diffusion of the Li-ion in the graphite matrix.

With the change of the electrode potential from 0.90 V to 0.12 V the semicircles are more pronounced.

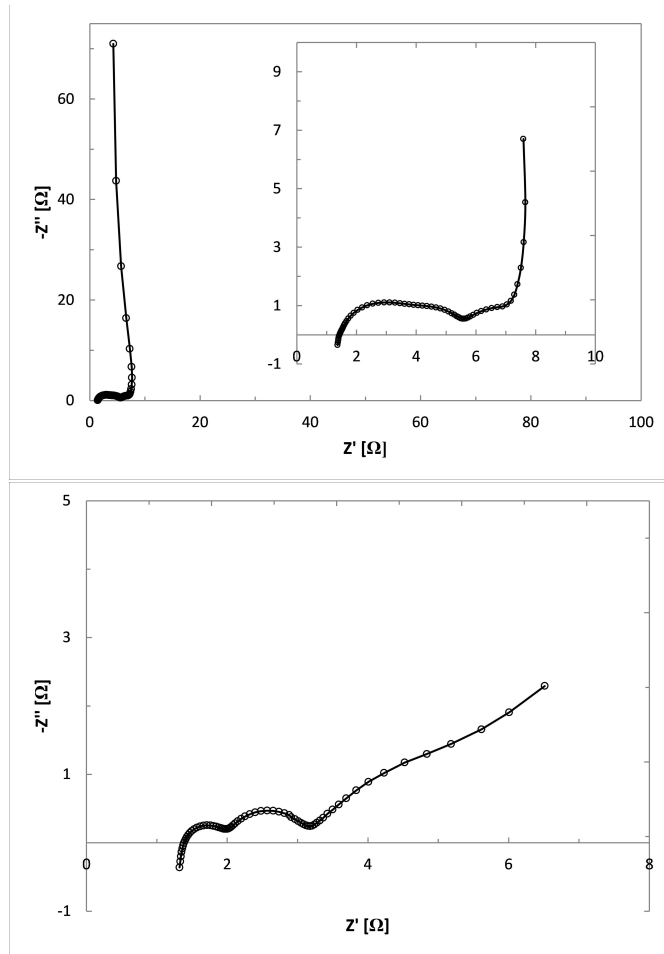


Figure 4.9: Nyquist plots of the graphite electrode at potentials 0.90 V (top) and 0.12 V (bottom) during the 7th cycle.

Figure 4.10 show Nyquist plots of the partially lithiated graphite electrode at potentials of 0.90 V and 0.12 V during the 17th lithiation (17. cycle) of the cell. Three spectra were recorded and averaged for each voltage.

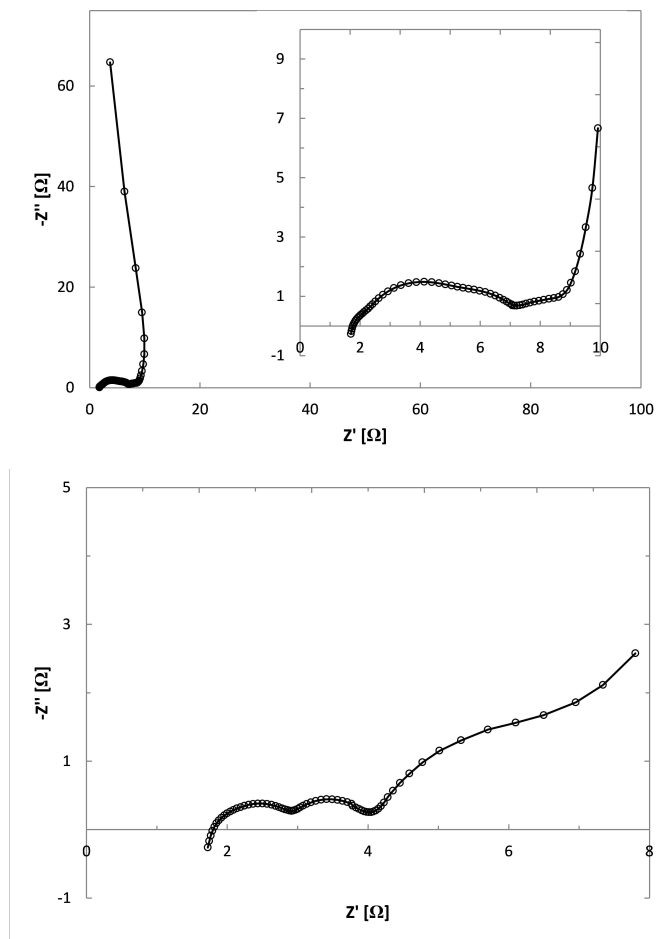


Figure 4.10: Nyquist plots of the graphite electrode at potentials 0.90 V (top) and 0.12 V (bottom) during the 17th cycle.

The Nyquist plots show the same features as those in Figure 4.9. An increase of the impedance after the prolonged cycling is clearly observed.

An equivalent circuit, as shown in Figure 4.11, was proposed to fit the frequency range 46.9 Hz to 1 MHz of the impedance spectra. A fit for the whole spectra was not found, because the software did not provide diffusion elements describing

diffusion/intercalation in spherical particles.

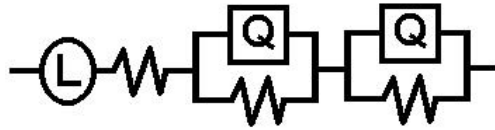


Figure 4.11: Equivalent circuit proposed for analysis of the frequency range 46.9 Hz to 1 MHz of the impedance spectra.

Figure 4.12 shows the simulated impedance spectra compared with experimental EIS data at 0.90 V after the initial cycling. The values of the parameters for all four cases are listed in Table 4.6 and Table 4.7. The uncertainties are relative standard errors. The low value of the χ^2 show that the proposed model describes the experimental data excellent in this frequency range.

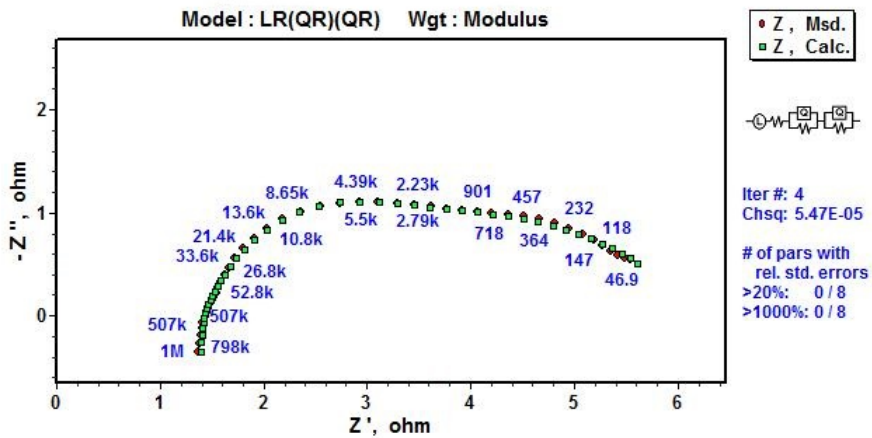


Figure 4.12: Comparison of EIS experimental data at 0.90 V during the 7th cycle with simulation results using the equivalent circuit of Figure 4.11.

Table 4.6: Equivalent circuit parameters obtained from fitting the experimental impedance spectra at 0.90 V during the 7th and 17th lithiation of the cell.

Parameters	Values, 7th cycle	Uncertainty [%]	Values, 17th cycle	Uncertainty [%]
L	6.41E-08	1.512	6.749E-08	1.845
R _e	1.345	0.3992	1.505	0.9704
Q ₁ - Y ₀	2.282E-05	18.1	3.005E-05	24.14
Q ₁ - n	1	2.173	1	3.284
R _{sei}	1.013	7.629	1.187	12.89
Q ₂ - Y ₀	0.002669	8.77	0.00403	19.6
Q ₂ - n	0.5492	1.08	0.4401	3.448
R _{ct}	3.842	1.89	5.748	1.44

Table 4.7: Equivalent circuit parameters obtained from fitting the experimental impedance spectra at 0.12 V during the 7th and 17th lithiation of the cell.

Parameters	Values, 7th cycle	Uncertainty [%]	Values, 17th cycle	Uncertainty [%]
L	6.224E-08	1.452	5.99E-08	2.607
R _e	1.331	0.3005	1.639	0.7992
Q ₁ - Y ₀	0.003496	8.491	0.004093	14.92
Q ₁ - n	0.79	1.727	0.7951	3.35
R _{sei}	1.252	1.927	1.066	4.38
Q ₂ - Y ₀	0.0001108	14.52	0.0004232	16.71
Q ₂ - n	0.7922	1.582	0.6104	2.385
R _{ct}	0.6639	2.097	1.396	2.9

As can be seen from Table 4.6 and Table 4.7 the electrolyte resistance is increased after the prolonged cycling, while the resistance of the SEI layer is approximately constant. The resistance of the SEI seems to neither depend on the voltage. The charge transfer resistance decreases when the potential is changed from 0.90 V to 0.12 V. After prolonged cycling the charge transfer resistance is increased (almost doubled). Q₁ is considerably increased when the potential is changed from 0.90 V to 0.12 V, while Q₂ is decreased. Both Q₁ and Q₂ is increased after the prolonged cycling. At 0.90 V the charge transfer resistance is the largest impedance, while at 0.12 V the electrolyte/contact resistance is the largest impedance.

4.4 Thermal analysis

In this section results from the thermal analysis will be presented. The analysis were performed in order to reveal the influence of the various parameters (graphite type, electrolyte and cycling rate) on the thermal stability of the samples. Three

parallel analysis were conducted for each combination of graphite, electrolyte and cycling rate. One representative DSC curve of each combination was chosen for presentation. The measured heat flow rates were normalized with the graphite weight (W/g). In the following figures exothermic reactions are displayed as upward responses.

Figure 4.13 shows DSC curves of pure electrolytes. Note that the baselines are not vertical straight lines, but lines with a slight negative slope. An endothermic response begins near 180 °C, followed by an exothermic response with peak temperature of ~245 °C. According to literature on the field, as described in chapter 2.7, the responses are caused by endothermic decomposition of EMC and exothermic decomposition of EC. The endothermic reaction of electrolyte E1 consumes more heat than the reaction of E2, as can be seen from the more pronounced endothermic peak of the former. On the other hand, the exothermic reaction of E2 produces more heat than the reaction of E1, as can be seen from the larger exothermic peak of the former. The reasons for this behaviours will be further discussed in chapter 5.4.

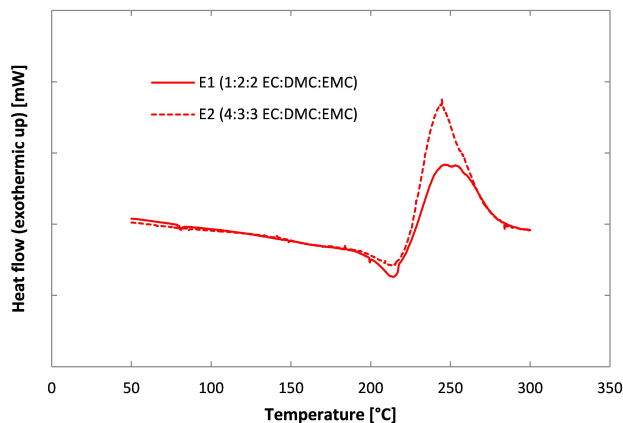


Figure 4.13: Comparison of the thermal behaviour of the pure electrolytes.

Figure 4.14 shows DSC curves of rapid and moderate cycled CPreme G8 with electrolytes E1 and E2, while Figure 4.15 compares the thermal stability of moderate cycled CPreme G8 and Elkem A2 (2650) samples with the E2 electrolyte. The baselines have slightly different slopes.

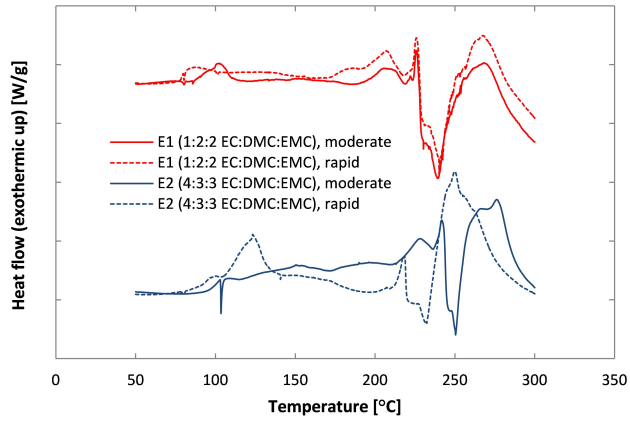


Figure 4.14: Comparison of the thermal behaviour of rapid and moderate cycled CPremeG8 electrode samples with electrolyte E1 and E2.

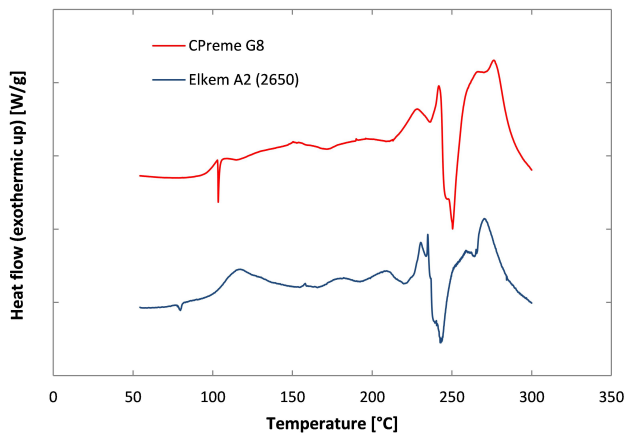


Figure 4.15: Comparison of the thermal behaviour of the moderate cycled graphite electrode samples with electrolyte E2.

The shape of the DSC curves show similar features as the the characteristic DSC curve reported by Haik et al. [6]. An exothermic response is seen below 100 °C, followed by a mild heat evolution between $\sim 100^\circ$ and $\sim 210^\circ$. According to the literature on the field, as described in chapter 2.7, the first exothermic response is due to SEI transformation, while the following mild heat evolution is due to continuous reaction between lithiated graphite and the electrolyte solution through the SEI layer. At about 210 °C there is increased heat evolution due to electrolyte decomposition. The following large endothermic peak is caused by exfoliation of the graphite structure. The last exothermic response is related to further thermal reactions of electrolyte species and their thermal products and at the same time to the thermal decomposition reactions of the PVDF binder.

The sharp endothermic peak at 103 °C in the DSC curve showing the response of moderate cycled CPreme G8 with electrolyte E2 is believed to be an artefact caused by the instrument, as this peak only occurred for this parallel.

There are some slight differences in the onset temperature of the SEI transformation in the DSC curves. The average onset temperatures of SEI transformation are given in Table 4.8. There is a tendency towards lower onset temperatures for Elkem A2 (2650) has the highest onset temperature, indicating that this graphite has a more stable SEI layer than the CPreme G8 graphite.

Table 4.8: Onset temperature of SEI transformation.

Material	Electrolyte	Cycling programme	Onset temperature [°C]
CPreme G8	E1	Rapid	85 ± 5
CPreme G8	E1	Moderate	80 ± 5
CPreme G8	E2	Rapid	93 ± 5
CPreme G8	E2	Moderate	95 ± 5
Elkem A2 (2650)	E2	Moderate	101 ± 5

Apart from the onset temperature, the DSC curves of CPreme G8 with the E1 electrolyte appear similar. The DSC curves of CPreme G8 with the E2 electrolyte, on the other hand, have some differences. The heat evolution due to decomposition of the electrolyte seems to occur at a lower temperature for the sample which are rapid cycled. The subsequent endothermic and exothermic responses also occur at lower temperatures for the rapid cycled sample. The differences will be further discussed in chapter 5.4.

The same features as those observed for cycled CPreme G8 (Figure 4.14 are also present in the DSC curves of moderate cycled Elkem A2 (2650) with electrolyte E2.

The onset temperature of the SEI formation is ~ 100 °C, which is slightly higher than the onset temperature of the CPreme G8 samples. The onset temperature and heat generation of the electrolyte decomposition and the graphite exfoliation seem to be similar for both samples. The possible explanations for these behaviours will be further discussed in chapter 5.4.

Chapter 5

Discussion

5.1 Materials characterization

The SEM pictures in Figure 4.1 (p. 42) showed that Elkem A2 (2650) contains particles with a more flaky morphology and rougher edges and surfaces than CPreme G8. Although the particles sizes appeared similar in the SEM pictures, the PSD measurements revealed that Elkem A2 (2650) consists of slightly larger particles than CPreme G8. The BET specific surface areas, as presented in Table 4.2 (p. 43), contradict the expected values from the PSD measurements. Elkem A2 (2650) has an approximately five times larger BET specific surface area than CPreme G8 ($9.7 \pm 0.1 \text{ m}^2/\text{g}$ vs. $1.79 \pm 0.03 \text{ m}^2/\text{g}$). Because Elkem A2 (2650) contains slightly larger particles than CPreme G8, this material should have the lowest specific surface area. It is obvious, however, that the rougher surfaces and edges on Elkem A2 (2650) contribute to an increased surface area, as compared to the smoother surface of CPreme G8.

Moreover, Elkem A2 (2650) has a more heterogeneous surface than CPreme G8. The relative extent of edge planes are approximately equal for both graphites. Elkem A2 (2650) has 17 % of the surface area made up of defects, while CPreme G8 do not contain any surface defects. The coating on CPreme G8 is a uniform, homogeneous, graphite-on-graphite surface coating. Such a coating should produce a homogeneous surface with a minimum of defects. This is reflected in Figure 4.2 (p. 44) in which only three different adsorptive potentials are seen, non of them corresponds to the adsorptive potential of defects ($> 62 \text{ K}$). Consequently, the

ratio of basal plane to non basal plane surface area is considerably higher for CPreme G8 than Elkem A2 (2650).

Due to the higher BET specific surface area Elkem A2 (2650) should have the largest ICL. In accordance with Placke et al.'s [25] findings the higher ratio of non basal plane to basal plane surface area of Elkem A1 (2650) should also result in a higher ICL for the Elkem material.

The DFT area is higher than the BET area, because the DFT method assumes that nitrogen adsorbs heterogeneously on basal and edge planes, and hence occupies different extents of the surface area.

5.2 Electrochemical measurements

The results from the long-term cycling (Figure 4.3 to Figure 4.7) show that the capacities are reduced when the C-rate is increased, but most of the capacity is retained when the rate is decreased. This is a well-known phenomenon for Li-ion batteries, related to the finite conductivity of the electrolyte of the batteries, which is insufficient to maintain a high flux of the reacting species towards the active electrode surface. A high charge rate, implying a high charge/discharge current, also causes a large potential drop across the electrode. Hence, the cut-off potential will be reached before the full capacity is obtained.

Some selected charging curves from the rapid cycling of CPreme G8 with electrolyte E1 (sample 2) and E2 (sample 1) are shown in Figure 5.1 and Figure 5.2, respectively. The other two samples of each combination showed similar behaviour as the ones presented. The vertical bars are the change in potential during the 2 minutes relax step after the cut-off voltage have been reached and the potential has been held at the cut-off voltage for 2 minutes.

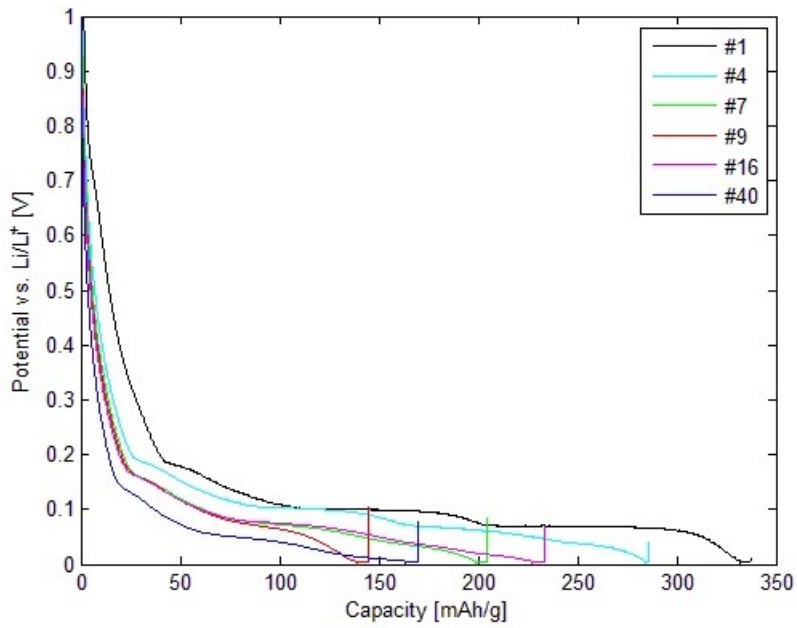


Figure 5.1: Selected charging curves from rapid cycling of CPreme G8 with electrolyte E1 (sample 2).

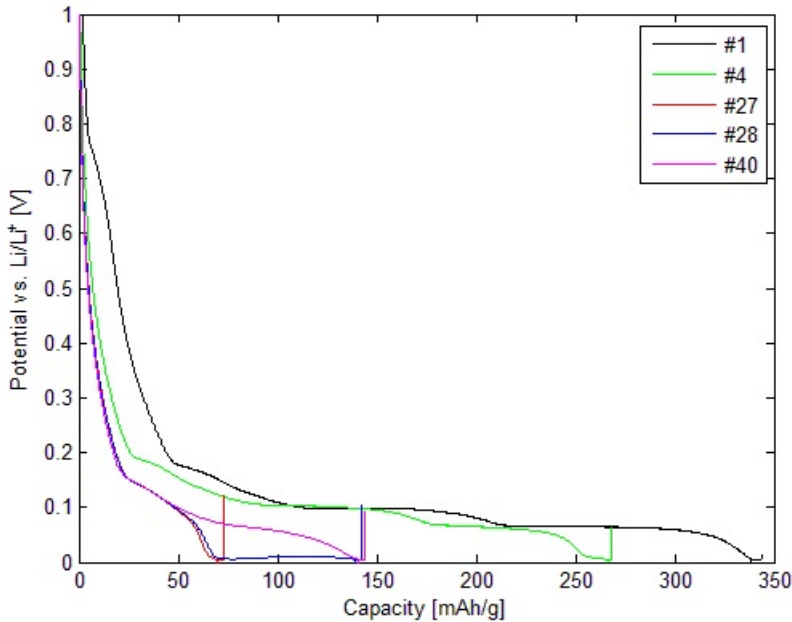


Figure 5.2: Selected charging curves from rapid cycling of CPreme G8 with electrolyte E2 (sample 1).

Several voltage plateaus are visible in the charging curves. The voltage plateau at ~ 0.8 V in the first lithium insertion half cycle is ascribed to the irreversible formation of the SEI layer on the carbon surface. The SEI formation continues from ~ 0.8 V to ~ 0.2 V versus Li/Li⁺. The voltage plateau at ~ 0.8 V is less pronounced for CPreme G8 with electrolyte E1 than for CPreme G8 with electrolyte E2, indicating less SEI formation for the former system.

Reversible Li-ion intercalation/de-intercalation occurs at potentials below ~ 0.2 V versus Li/Li⁺. The observed voltage plateaus in this potential range is related to the staging phenomenon and correspond to the phase transitions between the different stage- n phases during Li-ion intercalation/de-intercalation, as described in chapter 2.2.1. The transitions have been found to occur at 0.20, 0.14, 0.12 and 0.09 V respectively [12], which corresponds well with the observed behaviour of the lithiation curve obtained from cycle number 1. It should be noted that there is a shift in potential of the plateaus to lower values as the C-rate is increased.

The shift is especially large for cycle number 40 of the rapid cycled CPreme G8 with electrolyte E1.

The observed behaviour of the lithiation of cycle number 28 of the rapid cycled CPreme G8 with electrolyte E2 is noteworthy. Just before the potential reaches the cut-off at 5 mV, the voltage increases. The potential stays above the cut-off potential while the capacity is further increased, until the potential drops and reaches the cut off at 5 mV. This explains the observed behaviour in Figure 4.4, where the capacity increases rapidly during one cycle.

After the capacity is recovered again, CPreme G8 with electrolyte E1 experiences a steady capacity fade, while CPreme G8 with electrolyte E2 has a stable capacity. This might be related to the SEI stability. As described in chapter 2.4.1.2, EC is responsible for a stable SEI. At least 30 % EC is believed to be necessary to create a SEI mainly consisting of EC reduction products [26, 27]. Hence, electrolyte E1 with only 20 % EC might not be able to create a stable SEI, preventing further reduction and capacity fade.

Sample 3 of moderate cycled CPreme G8 with electrolyte E1 shows better performance than sample 1 and 2. This might be an effect of the higher porosity (69 % versus 64 % for the other two samples) and lower loading (~ 5 mg/cm² versus ~ 6 mg/cm² for the other two samples) of sample 3. This is clearly seen at a rate of C/2, as this sample show outstanding performance compared to the other two samples. As already explained, the electrolyte has a finite conductivity, which might be insufficient to maintain a high flux of the reacting species towards the active electrode surface. At high C-rates, the more porous structure and lower loading will have a better capability of maintaining a high flux of the reacting species towards the active electrode surface.

The performance characteristics of the materials was given in Table 4.4 (p. 49). It is evident from the table that Elkem A2 (2650) has the highest ICL of the investigated graphites, which corresponds well with the high BET specific surface area. A positive correlation between the BET specific surface area and the ICL has also been observed in the literature [22].

All samples experience a capacity fade during the long-term cycling. The SEM investigations did not reveal any cracks in the particle surfaces, hence this is not believed to be a cause for the capacity fade. After disassembling the coin cells traces of electrolyte was found between the Cu-foil and the battery case. This is believed to cause an increased contact resistance inside the batteries, which will increase the voltage drop and result in capacity fade, in particular at high rates. Other reasons for the capacity fade might be an increased charge transfer

resistance or and increased SEI resistance. According to literature, as described in chapter 2.5 the SEI might continue to grow during prolonged cycling, resulting in a thicker SEI layer with higher resistance. As the cycling experiments can not tell anything about the charge transfer resistance and/or the SEI resistance, the main causes for the capacity fade could not be revealed from these experiments.

For samples cycled at the same mode of cycling (rapid or moderate) the samples cycled with electrolyte E2 have a higher retained capacity than the samples cycled with electrolyte E1. As previously mentioned, electrolyte E1 is believed to have a lower viscosity and lower Li^+ desolvation energy than E2. Despite of this, E1 might not have as good SEI forming properties as E1, due to the lower amount of EC. This might affect the battery over time, as the SEI thickens and the impedance rises. Hence, the potential drops and the cut-off voltage is reached sooner.

5.3 Electrochemical impedance spectroscopy

The Nyquist plots in Figure 4.9 and Figure 4.10 show three semicircles. The shape of the curves is similar to those reported by Xu et al. (2011). They attributed both semicircles in the middle-frequency region to the charge transfer process. The authors explained this behaviour as a consequence of the nonhomogeneous layered structure of the porous graphite electrode and to the particle size distribution. The Nyquist plot simulated from their model describing an electrode with two different particle sizes showed similar shape as the semicircles in the Nyquist plots found in this work. Hence, there are reasons to believe that the two semicircles found in the middle-frequency area of the Nyquist plots are due to the porous structure and the particle size distribution of the electrodes.

As evidenced in Table 4.6 and Table 4.7 the parameter R_e , which is attributed to electrolyte and contact resistances, increases slightly during cycling. This might be due to a minor increase of the contact resistance or a slight degradation of the electrolyte conductivity.

The resistance of the SEI layer was found to be invariant of the potential, and it did not increase during the prolonged cycling. This indicates, in accordance with literature [26,27], that the SEI formed in the presence of electrolyte E2 is stable.

The charge transfer resistance was found to decrease when the potential was changed from 0.90 V to 0.12 V. A decreased charge transfer resistance upon increasing polarization is typical of electrochemical reactions. After prolonged

cycling the charge transfer resistance was increased (almost doubled). This is also reported in literature.

5.4 Thermal analysis

The DSC curves of pure electrolytes, shown in Figure 4.13, illustrates the thermal decomposition of the electrolyte components. The decompositions happens at the same temperatures, but the magnitudes of the heat evolutions are different. E1 consumes more heat than E2 during the decomposition of EMC, which is due to the higher amount of EMC in electrolyte E1 (40 % versus 30 %, respectively). E1 produces less heat than E2 during the decomposition of EC, which is due to the lower amount of EC in electrolyte E1 (20 % versus 40 %, respectively). The total amount of heat produced is less for E1 than E2, which would be favourable in a thermal runaway situation.

Figure 5.3 shows the thermal variation among two samples taken from the same graphite electrode. These curves demonstrate the degree of heterogeneity in the electrode. In addition, the instrument uncertainty should add to the total variation observed. Although the heat evolutions might be too different to draw conclusions about the amount of heat evolved in the samples, the onset temperatures seem to be fairly reliable.

The electrolyte compositions seem to have influenced the thermal stability of the SEI layer. The onset temperatures in Table 4.8 (p. 60) indicates that the CPreme G8 samples with electrolyte E1 has a slightly lower onset temperatures of SEI transformation than the samples with electrolyte E2, regardless of the cycling method. Hence, electrolyte E1 seem to be less thermally stable than electrolyte E2. There is reason to believe this might be related to the amount of EC in the electrolytes, as the electrolyte with 40 % EC seems to create the most stable SEI.

Moderate cycled Elkem A2 (2650) with electrolyte E2 has the highest onset temperature and hence is the system that shows the highest thermal stability of the investigated systems. This might be related to the amount of basal to non basal plane surface areas, which is higher for Elkem A2 (2650) than for CPreme G8. An earlier study by the author [41] and by others [42] indicated that there was a negative relation between the amount of basal planes and the onset temperature. One possible explanation for this might be that samples with a lower relative amount of edge planes might have a higher local concentration of Li^+ , hence shifting the reaction 2.10 to the right hand side, causing a lower onset

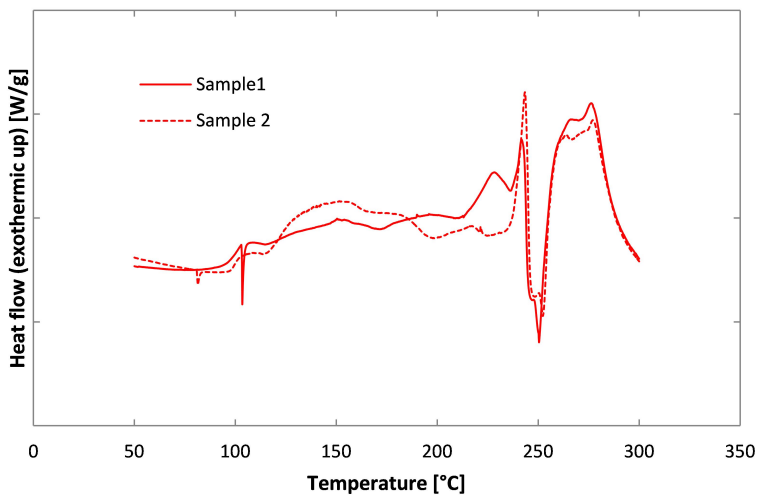


Figure 5.3: Example of thermal variation among two samples taken from the same graphite electrode (moderate cycled CPreme G8 with electrolyte E2).

temperature.

The DSC curve of rapid cycled CPreme G8 with electrolyte E2, as shown in Figure 4.14 (p. 59), deviates from the other curves. This deviation is assumed to originate from the sample preparation. The graphite electrode was left in the argon filled glow box over night, which might have caused oxidation of the lithium.

No explanation has been found for the lower onset temperature of exfoliation for CPreme G8 with electrolytes E1 as compared to moderate cycled CPreme G8 with electrolyte E2.

Moderate cycled CPreme G8 with electrolyte E2 seem to have a higher degree of exfoliation (larger endothermic peak at around 250 °C) than Elkem A2 (2650). As described in chapter 2.7, this might be due to the higher amount of basal to non basal planes of the former. The reduction of the graphite-Li-solvent intercalation compounds produces gas bubbles. A large size of the basal planes on the particle surface may lead to a longer diffusion path for the gas bubbles, which can result in a build-up of a higher pressure between the graphene layers and more enhanced exfoliation.

Chapter 6

Conclusion

Moderate cycled Elkem A2 (2650) with electrolyte E2 showed the best retained capacity (90.7 ± 1.0 %) upon long-term cycling. The CPreme G8 samples made with electrolyte E2 showed better retained capacity than the samples made with electrolyte E1, when the samples were cycled with the same cycling method. The electrolyte E2 is believed to create a more stable SEI than electrolyte E1, due to the higher amount of EC in the former electrolyte. The electrochemical impedance spectroscopy revealed that the SEI layer formed on CPreme G8 in the presence of electrolyte E2 was stable during prolonged cycling. In addition, EIS revealed that the capacity fade observed at long-term cycling might both be related to an increase in electrolyte and contact resistances and also to an increased charge transfer resistance.

Elkem A2 (2650) was found to be the most thermally stable material, due to its higher ratio of non basal to basal plane surface areas.

Bibliography

- [1] R. D. A. J. Dell Ronald M., *Understanding batteries*. The Royal Society of Chemistry, 2001.
- [2] F. Cheng, J. Liang, Z. Tao, and J. Chen, “Functional materials for rechargeable batteries,” *Adv Mater*, vol. 23, no. 15, pp. 1695–1715, 2011.
- [3] B. Scrosati and J. Garche, “Lithium batteries: Status, prospects and future,” *J Power Sources*, vol. 195, no. 9, pp. 2419–2430, 2010.
- [4] C. Liu, F. Li, M. Lai-Peng, and H.-M. Cheng, “Advanced materials for energy storage,” *Adv Mater*, vol. 22, no. 8, pp. E28–E62, 2010.
- [5] S. M. E. Novak Petr, Goers Dietrich, *Carbons for electrochemical energy storage and conversion systems*. CRC Press, 2010.
- [6] O. Haik, S. Ganin, G. Gershinsky, E. Zinigrad, B. Markovskiy, D. Aurbach, and I. Halalay, “On the thermal behavior of lithium intercalated graphites,” *J Electrochem Soc*, vol. 158, no. 8, pp. A913–A923, 2011.
- [7] J. Vetter, P. Novak, M. R. Wagner, C. Veit, K. C. Moller, J. O. Besenhard, M. Winter, M. Wohlfahrt-Mehrens, C. Vogler, and A. Hammouche, “Ageing mechanisms in lithium-ion batteries,” *Journal of Power Sources*, vol. 147, pp. 269–281, Sept. 2005.
- [8] C.-K. Back and J. Prakash, “Consideration of carbon structure effect on thermal stability of carbon anode for li ion rechargeable batteries,” *Thermochim Acta*, vol. 520, no. 1-2, pp. 93–98, 2011.
- [9] J. Kikkawa, T. Akita, M. Tabuchi, M. Shikano, K. Tatsumi, and M. Kohyama, “Real-space observation of li extraction/insertion in $\text{Li}_{1.2}\text{Mn}_{0.4}\text{Fe}_{0.4}\text{O}_2$ positive electrode material for li-ion batteries,” *Electrochem Solid State Letters*, vol. 11, no. 11, pp. A183–A186, 2008.

- [10] P. Verma, P. Maire, and P. Novak, "A review of the features and analyses of the solid electrolyte interphase in li-ion batteries," *Electrochim Acta*, vol. 55, no. 22, pp. 6332–6341, 2010.
- [11] J. Zheng, T. Dahn, *Carbon materials for advanced technologies*. Pergamon, 1999.
- [12] S. Flandrois and B. Simon, "Carbon materials for lithium-ion rechargeable batteries," *Carbon*, vol. 37, no. 2, pp. 165–180, 1999.
- [13] B. J. O. Winter Martin, *Lithium Ion Batteries - Fundamentals and Performance*. Wiley-VCH, 1998.
- [14] K. Kinoshita and K. Zaghbi, "Negative electrodes for li-ion batteries," *J Power Sources*, vol. 110, no. 2, pp. 416–423, 2002.
- [15] T. Tran, B. Yebka, X. Song, G. Nazri, K. Kinoshita, and D. Curtis, "Thermal and electrochemical studies of carbons for li-ion batteries 2. correlation of active sites and irreversible capacity loss," *J Power Sources*, vol. 85, no. 2, pp. 269–278, 2000.
- [16] K. Xu, *Encyclopedia of Electrochemical Power Sources*, ch. Secondary batteries - Lithium rechargeable systems — Electrolytes: Overview, pp. 51–70. Elsevier: Amsterdam, 2009.
- [17] P. Bernardo, J. Dentzer, R. Gadiou, W. Märkle, D. Goers, P. Novák, M. Spahr, and C. Vix-Guterl, "Influence of graphite surface properties on the first electrochemical lithium intercalation," *Carbon*, vol. 49, no. 14, pp. 4867–4876, 2011.
- [18] D. Aurbach, "The correlation between the surface chemistry and the performance of li-carbon intercalation anodes for rechargeable 'rocking-chair' type batteries," *Journal of the Electrochemical Society*, vol. 141(3), pp. 603–611, 1994.
- [19] U. V. R. Fong and J. Dahn, "Studies of lithium intercalation into carbons using nonaqueous electrochemical-cells," *Journal of the Electrochemical Society*, vol. 137(7), pp. 2009–2013, 1990.
- [20] J. Goodenough and Y. Kim, "Challenges for rechargeable li batteries," *Chem. Mater.*, vol. 22, no. 3, pp. 587–603, 2010.
- [21] K. Edström, M. Herstedt, and D. Abraham, "A new look at the solid electrolyte interphase on graphite anodes in li-ion batteries," *J Power Sources*, vol. 153, no. 2, pp. 380–384, 2006.

- [22] F. Joho, B. Rykart, A. Blome, P. Novak, H. Wilhelm, and M. Spahr, "Relation between surface properties, pore structure and first-cycle charge loss of graphite as negative electrode in lithium-ion batteries," *J Power Sources*, vol. 97-98, pp. 78–82, 2001.
- [23] H. Bryngelsson, M. Stjern Dahl, T. Gustafsson, and K. Edström, "How dynamic is the sei?," *J Power Sources*, vol. 174, no. 2, pp. 970–975, 2007.
- [24] T. Zheng, A. Gozdz, and G. Amatucci, "Reactivity of the solid electrolyte interface on carbon electrodes at elevated temperatures," *J Electrochem Soc*, vol. 146, no. 11, pp. 4014–4018, 1999.
- [25] T. Placke, V. Siozios, R. Schmitz, S. Lux, P. Bieker, C. Colle, H.-W. Meyer, S. Passerini, and M. Winter, "Influence of graphite surface modifications on the ratio of basal plane to "non-basal plane" surface area and on the anode performance in lithium ion batteries," *J Power Sources*, vol. 200, pp. 83–91, 2012.
- [26] K. Xu, "'charge-transfer" process at graphite/electrolyte interface and the solvation sheath structure of li +in nonaqueous electrolytes," *J Electrochem Soc*, vol. 154, no. 3, pp. A162–A167, 2007.
- [27] K. Xu, Y. Lam, S. Zhang, T. Jow, and T. Curtis, "Solvation sheath of li+ in nonaqueous electrolytes and its implication of graphite/electrolyte interface chemistry," *J. Phys. Chem. C*, vol. 111, no. 20, pp. 7411–7421, 2007.
- [28] J. Groot, *State-of-Health Estimation of Li-ion Batteries: Cycle Life Test Methods*. PhD thesis, Chalmers University of Technology, 2012.
- [29] K. Xu, A. Von Cresce, and U. Lee, "Differentiating contributions to "ion transfer" barrier from interphasial resistance and li+ desolvation at electrolyte/graphite interface," *Langmuir*, vol. 26, no. 13, pp. 11538–11543, 2010.
- [30] M. Broussely, P. Biensan, F. Bonhomme, P. Blanchard, S. Herreyre, K. Nechev, and R. Staniewicz, "Main aging mechanisms in li-ion batteries," *J Power Sources*, vol. 146, no. 1-2, pp. 90–96, 2005.
- [31] S.-D. Xu, Q.-C. Zhuang, L.-L. Tian, Y.-P. Qin, L. Fang, and S.-G. Sun, "Impedance spectra of nonhomogeneous, multilayered porous composite graphite electrodes for li-ion batteries: Experimental and theoretical studies," *J. Phys. Chem. C*, vol. 115, no. 18, pp. 9210–9219, 2011.
- [32] V. F. Lvovich, *Impedance Spectroscopy - Applications to Electrochemical and Dielectric Phenomena*. John Wiley & Sons, 2012.

- [33] Z. Stoyanov and D. Vladikova, *Encyclopedia of Electrochemical Power Sources*, ch. Measurement methods — Electrochemical: Impedance spectroscopy, pp. 632–642. Elsevier: Amsterdam, 2009.
- [34] S. Zhang, K. Xu, and T. Jow, “Eis study on the formation of solid electrolyte interface in li-ion battery,” *Electrochim Acta*, vol. 51, no. 8-9, pp. 1636–1640, 2006.
- [35] D. Aurbach, “Review of selected electrode-solution interactions which determine the performance of li and li ion batteries,” *J Power Sources*, vol. 89, no. 2, pp. 206–218, 2000.
- [36] J.-I. Yamaki, H. Takatsuji, T. Kawamura, and M. Egashira, “Thermal stability of graphite anode with electrolyte in lithium-ion cells,” *Solid State Ionics*, vol. 148, no. 3-4, pp. 241–245, 2002.
- [37] G. Gachot, S. Grugeon, G. Eshetu, D. Mathiron, P. Ribiere, M. Armand, and S. Laruelle, “Thermal behaviour of the lithiated-graphite/electrolyte interface through gc/ms analysis,” *Electrochim Acta*, vol. 83, pp. 402–409, 2012.
- [38] H.-J. G.W.H.Höhne, W.F.Hemminger, *Differential Scanning Calorimetry*. Springer, 2003.
- [39] *A Partial Cross Section of 2016 Coin cell, Hohsen Corporation*.
- [40] Illustration of Hohsen corp. 3E test cell. [cited 2013, 25th June]; Available from:.
- [41] I. Mattson, “Thermal and electrochemical stability of graphite anodes for li-ion batteries,” Master’s thesis, Norwegian University of Science and Technology, 2012.
- [42] Ø. Gullbrekken, “Thermal characterization of anode materials for li-ion batteries,” Master’s thesis, Department of Materials Science and Engineering, NTNU, 2012.